Fizika Nizkikh Temperatur, 1999, v. 25, No 8/9, p. 775–795

De Haas-van Alphen oscillation in both the normal and superconducting mixed states of $NbSe_2$, $CeRu_2$, URu_2Si_2, and UPd_2Al_3

(Review Article)

Y. Inada

Graduate School of Science, Osaka University, Toyonaka, Osaka 560-0043, Japan
E-mail: inaka@phys.sci.osaca-u.ac.jp

Y. Ōnuki

Graduate School of Science, Osaka University, Toyonaka, Osaka 560-0043, Japan
Advanced Science Research Center, Japan Atomic Energy Research Institute, Tokai, Ibaraki 319-1195, Japan
E-mail: onuki@phys.sci.osaca-u.ac.jp

Received March 22, 1999

The de Haas-van Alphen (dHvA) oscillation was observed clearly in both the normal and superconducting mixed states in $NbSe_2$, $CeRu_2$, URu_2Si_2, and UPd_2Al_3. The dHvA frequency, which is proportional to the extremal cross-sectional area of the Fermi surface, does not change in magnitude between the normal and mixed states. For the *f*-electron superconductors, the cyclotron effective mass is found to be reduced and the corresponding Dingle temperature or scattering rate of the conduction electron increases in the mixed state. An anisotropic energy gap with a line node for URu_2Si_2 and UPd_2Al_3 is discussed from the angular dependence of the dHvA amplitude in the mixed state.

PACS: **71.18.+y**, **74.70.–b**, 71.20.Lp

1. Introduction

Under a strong magnetic field the orbital motion of a conduction electron is quantized and forms Landau levels. The de Haas-van Alphen (dHvA) effect, which is caused when the Landau levels cross the Fermi energy by increasing the magnetic field, is a powerful method for determining the topology of the Fermi surface, the cyclotron effective mass m_c^* and the scattering lifetime τ of the conduction electron. This phenomenon was studied in the strongly correlated electron systems of the rare earth and uranium compounds, or so-called heavy fermion compounds [1]. In fact, the heavy mass of about 100 m_0 (m_0 is the rest mass of an electron) was detected by the dHvA effect in $CeRu_2Si_2$ [2] and UPt_3 [3,4]. The heavy fermion state is based on the hybridization effect between the conduction electrons with a wide energy band and the almost localized *f*-electrons. Especially, the Kondo effect is a basic phenomenon in the cerium and uranium compounds.

The many-body Kondo bound state is understood as follows. For the simplest case of no orbital degeneracy, the localized spin $\uparrow(l)$ is compensated by the conduction electron spin polarization $\downarrow(c)$. Consequently the singlet state $\{\uparrow(l)\downarrow(c) + \downarrow(l)\uparrow(c)\}$ is formed with the binding energy $k_B T_K$ relative to the magnetic state. Here, the Kondo temperature T_K is the single energy scale in the simple Kondo problem. In other words, disappearance of the localized moment is thought to be due to the formation of a spin-compensating cloud of the conduction electrons around the impurity moment.

The Kondo effect occurs independently at each cerium site even in a lattice system of the cerium compound such as $CeCu_6$ [1]. The ground-state properties of the Kondo lattice system are interesting with respect to magnetism. The electrical resistivity ρ follows a Fermi-liquid nature of $\rho = \rho_0 + AT^2$. The $\sqrt{A}$ value is extremely large, which correlates with an enhanced Pauli susceptibility $\chi \simeq \chi_0$ and a large electronic specific heat coefficient γ. In other words, the magnetic specific heat

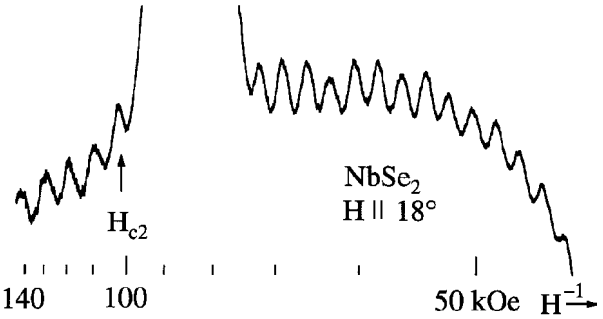

Fig. 1. De Haas-van Alphen oscillation in $NbSe_2$.

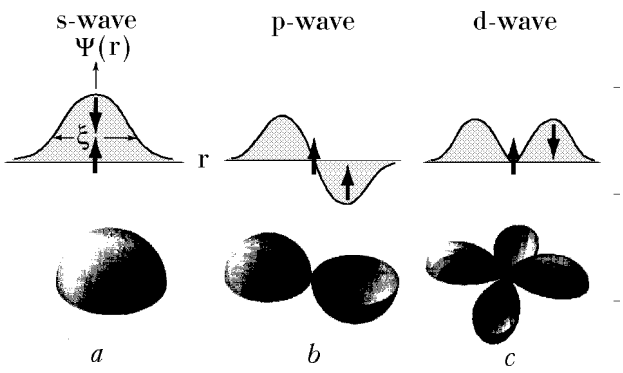

Fig. 2. Schematic view of the superconducting order parameter with the *s*-, *p*- and *d*-wave pairing.

of the *f*-electrons is changed into the electronic specific heat γT at low temperatures.

The dHvA effect was studied to clarify the heavy fermion state, as mentioned above. To our surprise, the dHvA oscillation was observed even in the superconducting mixed state of type II superconductors. The first measurement in the mixed state was done by Graebner and Robbins for a layered compound $NbSe_2$ by means of a magnetothermal technique [5]. Ōnuki et al. confirmed this oscillation by the measurement of the standard field modulation *ac* susceptibility [6,7].

Figure 1 shows the typical dHvA oscillation in both the normal and mixed states for $NbSe_2$. $NbSe_2$ is a conventional superconductor with a hexagonal structure. A transition temperature T_c is 7.2 K and the upper critical field H_{c2} is highly anisotropic; about 45 kOe for the field along the [0001] direction and 145 kOe for the field perpendicular to [0001]. In Fig. 1 the field is tilted by 18° from $[10\bar{1}0]$ to [0001], where H_{c2} is about 100 kOe. One dHvA oscillation with a frequency of $1.5 \cdot 10^6$ Oe is clearly observed even in the mixed state. The dHvA frequency, Dingle temperature and cyclotron mass did not obviously change between the normal and mixed states [6,7], although it was reported that only the Dingle temperature slightly increases with decreasing the field below H_{c2} [8].

Recently we have clearly observed the dHvA oscillation in *f*-electron superconductors $CeRu_2$ [9,10], URu_2Si_2 [11] and UPd_2Al_3 [12] in both the normal and superconducting mixed states. Till now, the dHvA oscillation in the mixed state has been observed for several compounds such as V_3Si, Nb_3Sn [8,13], YNi_2B_2C [14–16] as well as $NbSe_2$, $CeRu_2$, URu_2Si_2 [17] and UPd_2Al_3 mentioned above.

The most important issue for heavy fermion superconductors such as UPt_3 , URu_2Si_2 and UPd_2Al_3 is that superconductivity is realized in the antiferromagnetic state [18]. The superconducting properties such as the specific heat and the spin-lattice relaxation rate do not follow the exponential dependence of $e^{-\Delta/k_BT}$ which is expected from the BCS theory, but obey the power law of T^n. Here, Δ is the superconducting energy gap and n is an integer. These results are based on the fact that quasiparticles with heavy masses of 10–100 m_0 are of an *f*-electron character, as mentioned above, which originates from the strong Coulomb repulsion between the *f*-electrons. These quasiparticles condense into Cooper pairs.

When we compare the phonon-mediated attractive interaction to the strong repulsive interaction among the *f*-electrons, it is theoretically difficult for the former interaction to overcome the latter. To avoid a large overlap of the wave functions of the paired particles, the heavy fermion system would rather choose an anisotropic channel, like a *p*-wave spin triplet or a *d*-wave spin singlet state to form Cooper pairs. In fact, the heavy fermion superconductor exhibits antiferromagnetic ordering as mentioned above. Recent neutron scattering experiments clearly indicated evidence for a close relationship between superconductivity and magnetic excitation in UPd_2Al_3 [19,20]. A magnetic excitation gap, which appears in the inelastic neutron profile below T_c , corresponds to the superconducting order parameter.

Figure 2 shows a schematic view of the superconducting order parameter with the *s*-, *p*- and *d*-wave pairing. The order parameter $\mathbf{\Psi(r)}$ with even parity (*s*- and *d*-wave) is symmetric with respect to $\mathbf{r}$, where one electron with the up-spin state of the Cooper-pair is simply considered to be located at the center of $\mathbf{\Psi(r)}$, $\mathbf{r} = 0$ and the other electron with the down-spin state is located at $\mathbf{r}$. The width of $\mathbf{\Psi(r)}$ with respect to $\mathbf{r}$ is called the coherence length ξ, as shown in Fig. 2,*a*. UPd_2Al_3 is considered to be a *d*-wave superconductor from the NMR experiments, which is applied to the case in Fig. 2,*c* [21,22]. On the other hand, $\mathbf{\Psi(r)}$ with odd parity (*p*-wave) is not symmetric with respect to $\mathbf{r}$, where the parallel spin state is shown in Fig. 2,*b*. From

the NMR and magnetization experiments [23,24], UPt_3 is considered to possess odd parity in symmetry. Parity in URu_2Si_2 is not clear because almost all of the NMR-Knight shift was due to the orbital part, while the contribution of the spin part of the conduction electron was not detected [25].

The dHvA voltage V_{osc} is obtained by the method of 2ω detection of the field modulation [1];

$$V_{osc} = A \sin\left(2\pi \frac{F}{H} + \varphi\right), \qquad (1)$$

$$A \propto J_2(x) T H^{-1/2} \left|\frac{\partial^2 S}{\partial k_H^2}\right|^{-1/2} \frac{\exp(-\alpha m_c^* T_D/H)}{\sinh(\alpha m_c^* T/H)} \times$$

$$\times \cos\left(\frac{1}{2}\pi g \frac{m_c^*}{m_0}\right),$$

$$x = 2\pi \frac{Fh}{H^2}, \quad \alpha = \frac{2\pi^2 c k_B}{e\hbar},$$

where $J_2(x)$ is the Bessel function, which depends on the dHvA frequency F, the modulation field h and the magnetic field strength H. The dHvA frequency F [$= (c\hbar/2\pi e)S_F$] is proportional to the extremal (maximum or minimum) cross-sectional area S_F of the Fermi surface. The quantity $|\partial^2 S/\partial k_H^2|^{-1/2}$ is the inverse square root of the curvature factor $\partial^2 S/\partial k_H^2$, where the rapid change of the cross-sectional area around the extremal cross-sectional area along the field direction diminishes the dHvA amplitude for this extremal area. We can determine the cyclotron mass m_c^* from the temperature dependence of the dHvA amplitude A, namely, from the slope of a plot of $\ln A[1 - \exp(-2\alpha m_c^* T/H)]/T$ vs T at constant H and h by using a method of successive approximations, and we can obtain the Dingle temperature T_D [$= (\hbar/2\pi k_B)\tau^{-1}$] or the scattering lifetime τ from the field dependence of the amplitude, namely, from the slope of a plot of $\ln [AH^{1/2} \sinh(\alpha m_c^* T/H)/J_2(x)]$ vs H^{-1} at constant temperature. Here, g is the g-factor of the conduction electron, which is 2 for the free electron.

The dHvA oscillation is detected when the high-field condition is satisfied; $\omega_c\tau/2\pi > 1$, and the spacing between the Landau levels is larger than the thermal broadening $k_B T$; $\hbar\omega_c > k_B T$. If the magnetic field H is 100 kOe and the carrier possesses a cyclotron mass of 10 m_0, the following conditions for the temperature and the scattering lifetime are required: $T < 1.3$ K and $\tau > 3.6 \cdot 10^{-11}$ s or $T_D < 0.03$ K. A temperature of 0.4 K can be attained in the ^{3}He-cryostat and much lower temperatures are also obtainable in a dilution refrigerator. The typical Dingle temperature of a high-quality sample in the f-electron system is about 0.1 K, and thus fields higher than 100 kOe are necessary to detect the dHvA amplitude of the heavy conduction electron.

We have continued growing high-quality single crystals of f-electron superconductors such as $CeRu_2$, URu_2Si_2 and UPd_2Al_3, and extended our investigations on the dHvA experiments. The dHvA oscillation for these compounds has been observed in both the normal and superconducting mixed states. The field dependence of the cyclotron mass and the Dingle temperature in the mixed state is clarified in this paper. An anisotropic energy gap with a line node is also discussed on the basis of the angular dependence of the dHvA amplitude in the mixed state.

2. Theoretical

Maki [26], Wasserman and Springford [27], Dukan and Tešanović [28], Vavilov and Mineev [29] and Gor'kov and Schrieffer [30] have discussed theoretically the dHvA oscillation in the mixed state on the basis of the quasiparticles in magnetic fields. They claim that the dHvA frequency is unchanged from the normal state, but the amplitude is reduced by an additional quasiparticle scattering rate or the Dingle temperature, depending on the field and temperature. These characteristic features have been confirmed by the results of experiments for those compounds mentioned above.

For example, we have confirmed for $CeRu_2$, URu_2Si_2 and UPd_2Al_3 that the dHvA frequency is unchanged and the following simple relation holds between the Dingle temperature in the mixed state $\tilde{T}_D$ and the one in the normal state T_D : $\tilde{T}_D = T_D + \Delta T_D$, where ΔT_D is the additional Dingle temperature in the mixed state [10]. Moreover, the mass is found to decrease with decreasing field below H_{c2}. No report on the change of the mass has been done for the other superconductors. The change in the mass might be found in the highly correlated electron systems because $CeRu_2$, URu_2Si_2 and UPd_2Al_3 are f-electron superconductors with large effective masses. Experimentally, the dHvA oscillation in the mixed state can be most likely detected for any superconductor if its upper critical field H_{c2} is large enough, for example, more than about 30 kOe, and the single crystalline sample is of high quality. We shall explain briefly the reason why the dHvA oscillation is observed in the mixed state, considering a conventional superconductor of $CeRu_2$ with a cubic structure.

When the field is applied in a normal-state metal, the quasi-continuum momentum energy of the conduction electrons with up- and down-spin states is changed into the discrete energy levels, the so-called Landau levels. The dHvA oscillation is caused when the Landau levels cross the Fermi energy by increasing the field. Two scenarios might exist to explain the dHvA effect in the mixed state, where the dHvA oscillation is caused either by quasiparticles or by the Cooper-pair electrons. It is not certain whether each electron in the Cooper-pair could be quantized in energy by fields, while remaining the Cooper-pair with $(k, \uparrow)$ and $(-k, \downarrow)$ at 0 K. On the other hand, the de-paired electrons due to magnetic fields, namely, the quasiparticles could be quantized into Landau levels as in the usual normal-state metal. We shall discuss the latter case [10].

There exist three reduction factors in the dHvA oscillation. One is an inhomogeneous field due to vortices. The second is the electron scattering at the boundary between the normal region and the superconducting one, called the Andreev reflection. The last is the field dependence of the carrier concentration of the quasiparticles.

We shall examine the mixed state based on the Ginzburg-Landau (GL) theory. The order parameter $\Psi(\mathbf{r})$ and the microscopic magnetic field $\mathbf{h}(\mathbf{r}) = \nabla\times\mathbf{A}(\mathbf{r})$ in the mixed state are determined by solving the GL equations for $\Psi(\mathbf{r})$ and $\mathbf{A}(\mathbf{r})$ [31]. We rewrite the GL equations in terms of $\psi(\mathbf{r}) = |\Psi(\mathbf{r})|$ and $h(\mathbf{r})$ as

$$-\xi^2\nabla^2\psi(\mathbf{r}) + \frac{\lambda^2}{2H_c^2}\left(\frac{\nabla h(\mathbf{r})}{\psi^2(\mathbf{r})}\right)^2 \psi(\mathbf{r}) - \psi(\mathbf{r}) + \psi^3(\mathbf{r}) = 0 , \quad (2)$$

$$-\lambda^2\,\nabla\cdot\left(\frac{\nabla h(\mathbf{r})}{\psi^2(\mathbf{r})}\right) + h(\mathbf{r}) = \Phi_0 \sum_n \delta(\mathbf{r} - \mathbf{r}_n) , \quad (3)$$

where $\mathbf{r}_n$ is the position of the vortex center, H_c is the thermodynamic critical field, Φ_0 is the fluxoid, ξ is the coherence length, λ is the penetration depth. Applying the boundary condition $\psi(\mathbf{r}_n) = 0$ at the vortex center and the periodic boundary condition at the boundary of the unit cell of the vortex lattice, we solve Eqs. (2) and (3) numerically for $\kappa = \lambda/\xi = 25$, self-consistently by the relaxation method and considering $CeRu_2$.

We show in Fig. 3 the spatial dependence of the order parameter $\psi(\mathbf{r})$ or $|\Psi(\mathbf{r})|$, where ξ is the coherence length of 79 Å. At a low field of $H/H_{c2} = 0.1$, the vortices are separated enough and the order parameter between vortices is near to unity. On the other hand, at a high field of $H/H_{c2} = 0.7$, vortices

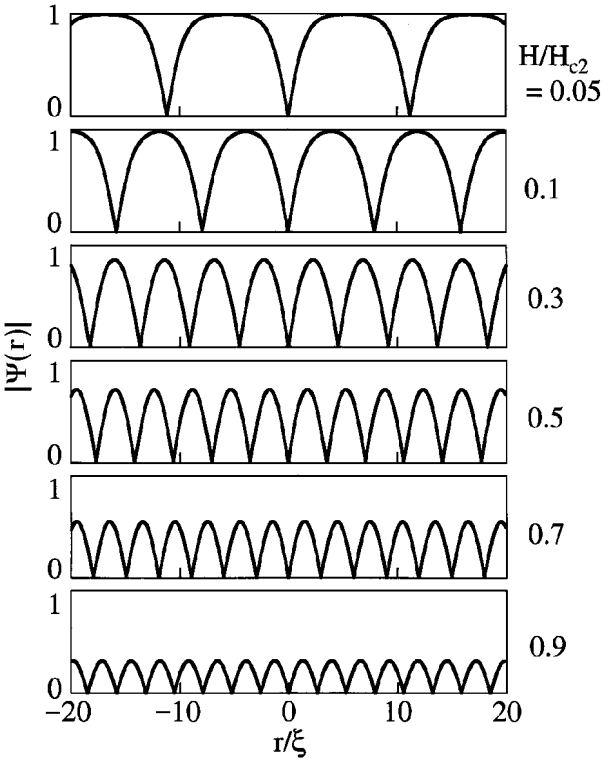

Fig. 3. Spatial dependence of the order parameter $|\Psi(\mathbf{r})|$ at several fields.

are numerous and the order parameter decreases almost by half. In the latter high field condition, the quasiparticles could circulate the cyclotron orbits in real space. Figure 4 shows a schematic Abrikosov lattice of the vortices and the cyclotron orbits at $H/H_{c2} = 0.7$. Each vortex with a diameter of 2ξ (= 158 Å) is separated by 255 Å at $H/H_{c2} = 0.7$. The corresponding cyclotron orbits in real space are illustrated for branches $\varepsilon_{1,2,3}$, δ and α with diameters of 1720, 3950 and 9440 Å, respectively, for $CeRu_2$.

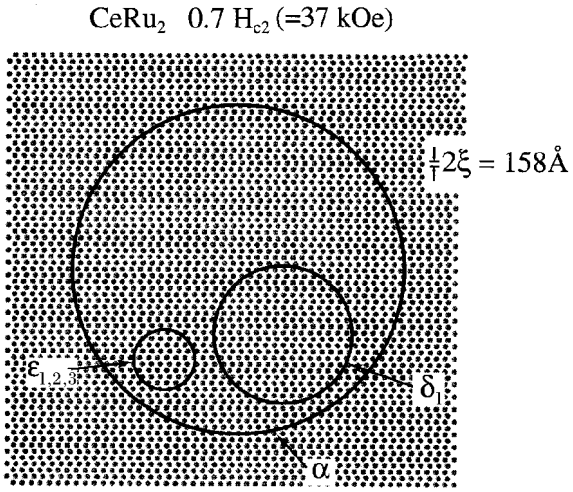

Fig. 4. Schematic Abrikosov lattice of the vortices and the cyclotron orbits at $H/H_{c2} = 0.7$ in $CeRu_2$.

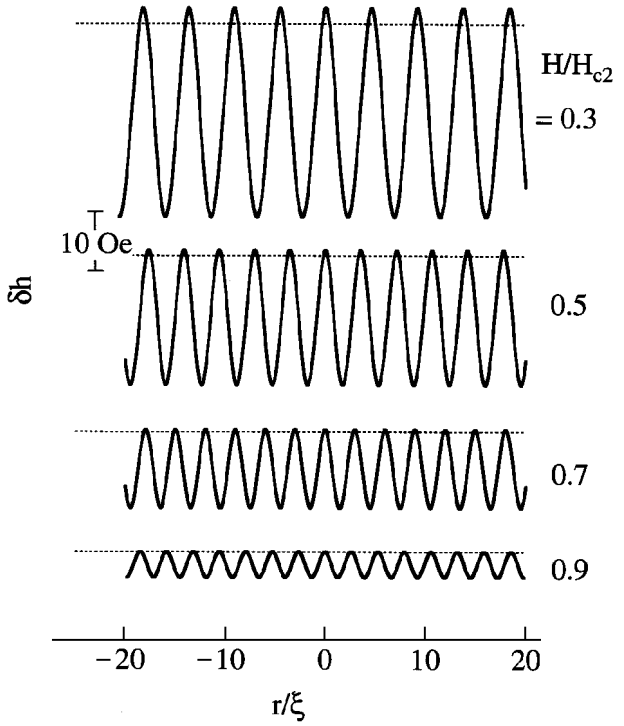

Fig. 5. Spatial variation of the magnetic field in $CeRu_2$.

The quasiparticles have to tunnel into the superconducting region in order to complete the cyclotron motion, which is prevented by the so-called Andreev reflection at a low field of $H/H_{c2} = 0.1$. The high field condition, for example, $H/H_{c2} > 0.1$ is necessary to complete the cyclotron motion, as mentioned above. Experimentally, the lowest fields to detect the dHvA oscillation in the mixed state are 0.6 H_{c2} for V_3Si [8], 0.2 H_{c2} for YNi_2B_2C [14], 0.4 H_{c2} for branch $\varepsilon_{1,2,3}$ for $CeRu_2$ [10], 0.4 H_{c2} for URu_2Si_2 [11] and 0.7 H_{c2} for UPd_2Al_3 [12].

Next we discuss inhomogeneity of the magnetic field $\delta h(\mathbf{r})$ defined by $\delta h(\mathbf{r}) = h(\mathbf{r}) - H$. Figure 5 shows the spatial inhomogeneity of the magnetic field in the superconductor at $H/H_{c2} = 0.3$, 0.5, 0.7 and 0.9. Inhomogeneous fields at $H/H_{c2} = 0.3$, 0.5, 0.7 and 0.9 are 35, 23, 13 and 4 Oe, respectively. The field H is shown by a horizontal dotted line in Fig. 5.

We note that a field interval for one cycle of the dHvA oscillation is 1880 Oe for branch ε, 340 Oe for δ and 60 Oe for α at $H = 0.7\ H_{c2}(= 37$ kOe). If this inhomogeneous field is directly related to the dHvA oscillation, the oscillation of branch α will be reduced in amplitude. This inhomogeneous field might not reduce the dHvA amplitude directly if the vortices formed a regular lattice.

An additional effective scattering rate in the mixed state $\delta\tau^{-1}$ is estimated by the uncertainty principle of $\delta\tau^{-1} \approx v_F \delta k_F$, where δk_F is variation in radius of the orbit cutting the same flux and v_F is Fermi velocity [13]. The area of the cyclotron orbit A is changed into $A + \delta A$ by the inhomogeneity of the field δh:

$$A + \delta A = \pi \left(\frac{m^* v_F\, c}{e(H + \delta h)} \right)^2 = \pi \left(\frac{m^* v_F\, c}{eH} \right)^2 -$$

$$- 2\pi \left(\frac{m^* v_F\, c}{eH} \right)^2 \frac{\delta h}{H} = \pi r^2 - 2\pi r^2 \frac{\delta h}{H}\,, \qquad (4)$$

where r is the radius of the cyclotron orbit. By using $\delta A = 2\pi r \delta r$, we can get the following relation:

$$\frac{2\pi r^2 \delta h}{H} = 2\pi r \delta r \quad \text{or} \quad \delta r = r \frac{\delta h}{H}\,. \qquad (5)$$

Therefore, the final relation is obtained from Eq. (5),

$$\delta k_F = \left(\frac{eH}{c\hbar} \right) \delta r \approx \frac{re\delta h}{c\hbar}\,. \qquad (6)$$

From the calculated values of δh mentioned above and Eq. (6), $\delta\tau^{-1}$ for $H/H_{c2} = 0.7$ is estimated to be of the order of 10^8 s^{-1} for branches α, δ_1 and $\varepsilon_{1,2,3}$. This value corresponds to a small value of δT_D, being of the order of 10^{-2} K. Inhomogeneity in the field is thus a minor reduction factor.

Using Maki's theory [26], we shall explain the change in the Dingle temperature and the mass in the mixed state. The Dingle temperature in the mixed state $\tilde{T}_D$ was given as the imaginary part of the self-energy for the quasiparticles in the mixed state close to H_{c2}:

$$\tilde{T}_D = T_D + \Delta T_D\,, \qquad (7)$$

$$\Delta T_D = \frac{\Delta^2(H, T)}{\sqrt{\pi}\, k_B \alpha}\,, \qquad (8)$$

$$\alpha = v_F \sqrt{2e\hbar H/c}\,, \qquad (9)$$

$$\Delta^2(H, T) = \Delta^2(T)\,(1 - H/H_{c2})\,, \qquad (10)$$

where T_D is the Dingle temperature in the normal state, ΔT_D is an additional one, v_F is Fermi velocity which is given as $\sqrt{2e\hbar F/c}/m_c^*$, and $\Delta(T)$ is the temperature-dependent BCS energy gap in zero field.

The effective mass of the quasiparticles in the mixed state $\tilde{m}_c^*$ was not given theoretically by Maki. We have calculated it by using the following formula [32]:

$$\tilde{m}_c^* = m_c^* \left[\frac{1 - \partial \Sigma_R(\xi, \omega)/\partial\omega}{1 + \partial \Sigma_R(\xi, \omega)/\partial\xi} \right]_{\xi=0,\ \omega=0}, \quad (11)$$

where $\Sigma_R(\xi, \omega)$ is the real part of the self-energy for the quasiparticles in the mixed state, and ξ and m_c^* are the quasiparticle's energy measured relative to the Fermi energy and the effective mass in the normal state, respectively. The energy ω is also measured relative to the Fermi energy and therefore $\omega = 0$ corresponds to the Fermi energy. Using the self-energy derived by Brandt et al. [33],

$$\Sigma(\xi, \omega) = \Delta^2(H, T) \int_{-\infty}^{\infty} \frac{du}{\sqrt{\pi}} \frac{e^{-u^2}}{\omega + i\delta + \xi - \alpha u}, \quad (12)$$

we obtain the cyclotron effective mass in the mixed state $\tilde{m}_c^*$ as

$$\tilde{m}_c^* = m_c^* \frac{1 - 2(\Delta(H, T)/\alpha)^2}{1 + 2(\Delta(H, T)/\alpha)^2} \simeq m_c^* \frac{1}{1 + 4(\Delta(H, T)/\alpha)^2}. \quad (13)$$

A Maki's theory is based on a mixed state self-energy calculated by Brandt et al. [33]. They clarified the spatially averaged density of states of type II superconductors in fields. Figure 6 shows the energy dependence of the density of states $D_s(\omega)$ in the pure limit, which was calculated by Brandt et al. As mentioned above, the energy at $\omega = 0$ corresponds to the Fermi energy. $D_s(\omega)$ in the energy range of $\omega/\Delta_0 = 0$ to 1 is zero at zero field but increases with increasing the field, reaching an ω-independent value of D_0 at H_{c2}.

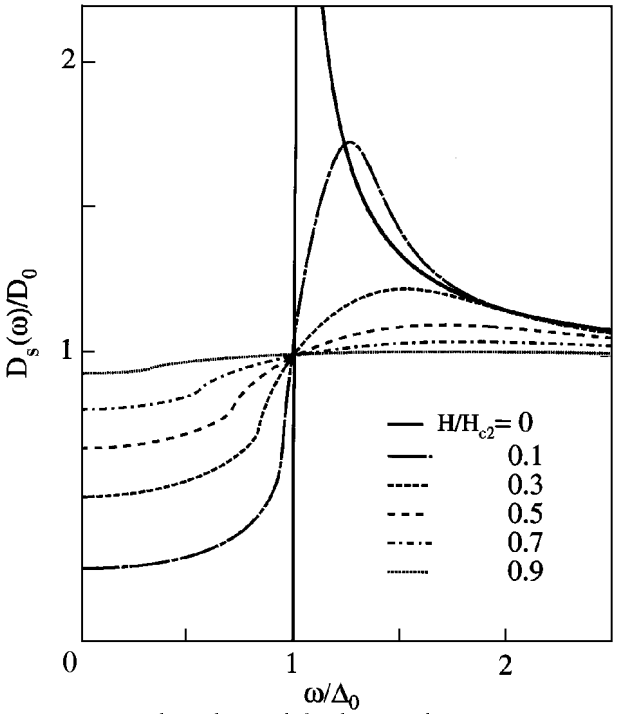

Fig. 6. Energy dependence of the density of states $D_s(\omega)/D_0$ in the pure limit.

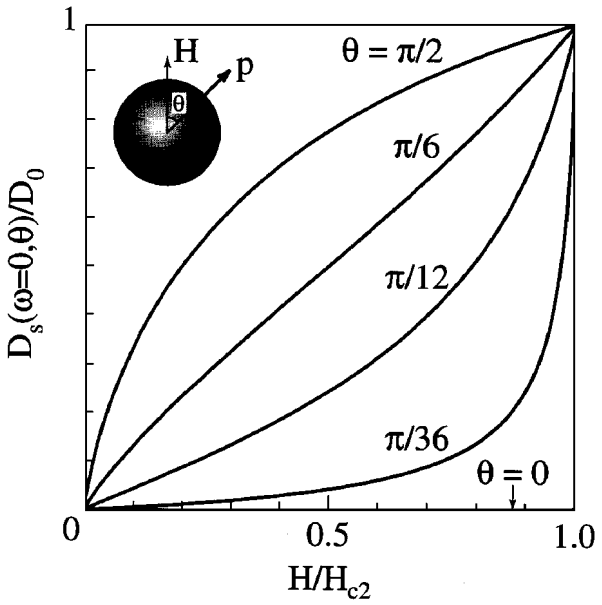

Fig. 7. Field dependence of the density of states in the mixed state for several polar angles.

The density of states is found to vary from the «gapless» state to the BCS type as the angle θ changes from $\pi/2$ to zero. Figure 7 shows the field dependence of the density of states at the Fermi energy ($\omega = 0$) in the mixed state for several angles. Here, the angle θ is the polar angle of the quasiparticle momentum $\mathbf{p}$ with respect to the direction of the magnetic field, as shown in an inset of Fig. 7. The Maki's theory corresponds to the $\theta = \pi/2$ case because α in Eq. (9) is changed into $\alpha = v_F \sin\theta \sqrt{2e\hbar H/c}$ for the angle θ. $D_s(\omega)$ in Fig. 6 is also the total density of states, namely, an average over the angle θ of 0 to $\pi/2$.

$D_s(\omega = 0, \theta)$ in fields possesses a finite value for any angle except $\theta = 0$, corresponding to the gapless state mentioned above. In particular, $D_s(\omega = 0, \theta = \pi/2)/D_0$ is 0.85 at 0.7 H_{c2} or 37 kOe in

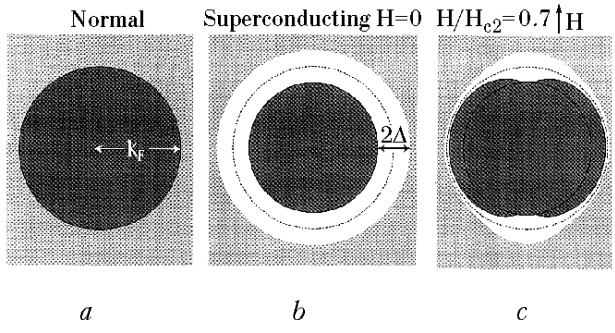

Fig. 8. Schematic superconducting energy gap in $H/H_{c2} = 0$ and 0.7.

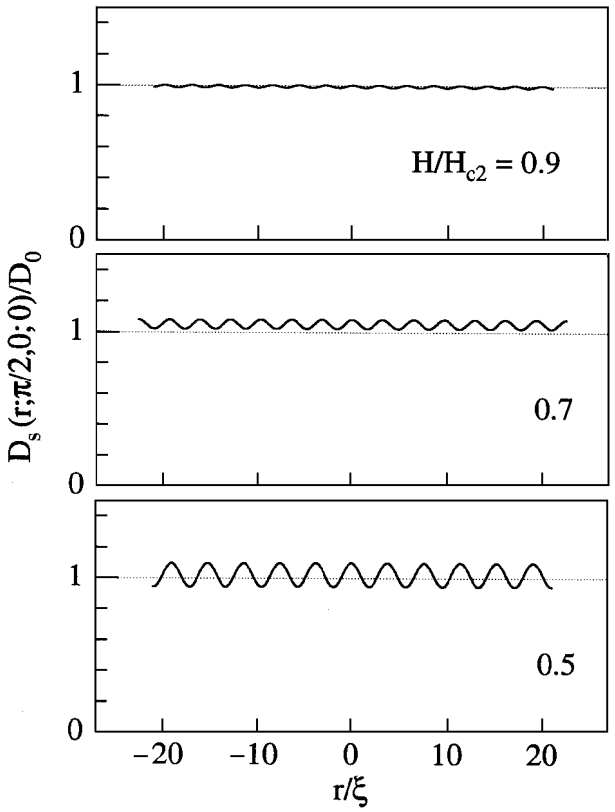

Fig. 9. Local density of states for the quasiparticles along the direction connecting the neighboring vortices.

$CeRu_2$. The angle $\theta = \pi/2$ corresponds to a maximum area of the spherical Fermi surface S_F in the dHvA oscillation, as schematically shown in Fig. 8. This is the reason why the dHvA oscillation can be detected in the mixed state.

Lastly we discuss the local density of states. The local density of states for the quasiparticles propagating in the direction of $\mathbf{v}_F = v_F(\sin\theta\cos\varphi, \sin\theta\sin\varphi, \cos\theta)$, where φ is the azimuthal angle in the plane perpendicular to the magnetic field, is calculated by the formula

$$D_s(\mathbf{r};\ \theta,\ \varphi;\ \omega) =$$

$$= -\frac{1}{\pi} D_0 \sum_i \int_{-\infty}^{\infty} d\xi_p \ \mathrm{Im}\,[G_\omega(\mathbf{p},\ \mathbf{K}_i)]\ e^{i\mathbf{K}_i\cdot\mathbf{r}}\ , \quad (14)$$

where $G_\omega(\mathbf{p},\ \mathbf{K}_i)$ are the quasiparticle Green's functions calculated from the Gor'kov equation and $\mathbf{K}_i$ are the reciprocal lattice vectors of the vortex lattice. Assuming the Abrikosov solution for the order parameter, we can solve the Gor'kov equation numerically for $G_\omega(\mathbf{p},\ \mathbf{K}_i)$.

The density of states averaged over r, θ and φ may be calculated by using the Green's function with $\mathbf{K} = 0$ alone, as done by Brandt et al. However, in order to calculate the spatial variation of the density of states in the mixed state, it is crucial to incorporate Green's functions with $\mathbf{K} \neq 0$. Thus we take into account the reciprocal lattice vectors of $\mathbf{K}_0 = 0$ and 60 vectors $(\mathbf{K}_1, \ldots, \mathbf{K}_{60})$ surrounding $\mathbf{K}_0$, and calculate the Green's functions with the $\mathbf{K}_i$'s.

In relation with the dHvA effect, we are interested in the quasiparticles propagating in the plane perpendicular to $\mathbf{H}$ ($\theta = \pi/2$), particularly along the line connecting the neighboring vortices where the direction of the line is chosen to be $\varphi = 0$. In Fig. 9 we show the local density of states at the Fermi level $D_s(\mathbf{r};\ \pi/2,\ 0;\ 0)$ for $H/H_{c2} = 0.5$, 0.7 and 0.9. The densities of states for $H/H_{c2} = 0.5$, 0.7 and 0.9 are close to the value in the normal state and their modulation is rather small. Unexpectedly, in the intermediate fields of $H/H_{c2} = 0.5$ and 0.7, the density of states is enhanced comparing to that at 0 K in the normal state, indicating the suppression of $D_s(\mathbf{r};\ \pi/2,\ \varphi;\ 0)$ in other directions. This enhancement persists down to $\sim 0.2H_{c2}$. This is the reason why the dHvA effect is observed even at low fields of $0.2H_{c2}$ as in YNi_2B_2C.

As mentioned in Sec. 1, the NMR and specific heat experiments predict the anisotropic energy gap with a line node in uranium-based heavy fermion superconductors such as URu_2Si_2 and UPd_2Al_3 . They are unconventional superconductors. Figure 10 shows an energy gap with a line node of a so-called polar type. As mentioned above, S_F is the extremal area of cross-section of the Fermi surface by planes perpendicular to the field direction. If S_F corresponds to the maximum cross-section with the line node (polar type) shown in Fig. 10,*a* and *b*, it is not easy to distinguish experimentally the line node in the anisotropic energy gap from the gapless state based on the pair-breaking by applying the magnetic fields. In this case, it is necessary to

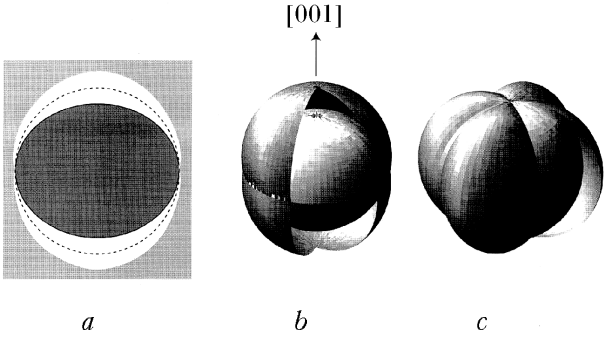

Fig. 10. Schematic superconducting energy gap with a line node. (*a*) and (*b*) The line node exists along the equator. (*a*) in the cross-section of (*b*). In (*c*), there exist two line nodes crossing poles.

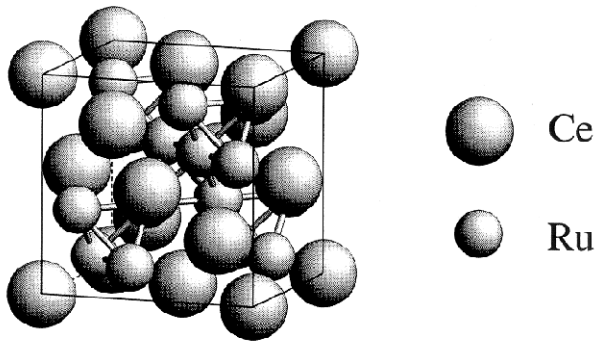

Fig. 11. Crystal structure of $CeRu_2$.

deviate S_F from the cross-section with the line node by tilting the field direction. It is thus a challenging study to detect the line node in the anisotropic energy gap for URu_2Si_2 and UPd_2Al_3 via the dHvA oscillation in the mixed state.

3. Experimental results and discussion

3.1. $CeRu_2$

A single crystals of $CeRu_2$ with the cubic Laves-phase structure was grown by the Czochralski method in a tetra-arc furnace. Figure 11 shows the crystal structure of $CeRu_2$. An as-grown ingot of 3–4 mm in diameter and 60 mm in length was annealed at 700–800 °C under vacuum of 10^{-10} Torr by means of the electro-transport method. Figure 12 shows the temperature dependence of the electrical resistivity. The residual resistivity ρ_0 was estimated as 0.6 μΩ·cm by using a Fermi-liquid formula $\rho = \rho_0 + A T^2$, and the residual resistivity ratio ρ_{RT}/ρ_0 was 270, indicating a high-quality sample. Superconductivity occured below $T_c = 6.4$ K.

$CeRu_2$ is a conventional type II-superconductor because the coherence peak at T_c is clearly observed in the NMR experiment [34], and the spin-lattice relaxation rate in NMR and the specific heat follow an exponential law in the temperature dependence [35]. The superconducting properties are summarized in Table 1. Values of the upper critical field at 0 K $H_{c2}(0)$, thermodynamic critical field $H_c(0)$ and lower critical field $H_{c1}(0)$ shown in Table 1 have been directly determined from the specific heat and magnetization experiments [35]. The other physical values are estimated from the conventional relations $H_{c2} = \Phi_0/2\pi\xi^2$, $\kappa = \lambda/\xi$ and $H_{c2} = \kappa\sqrt{2}\, H_c$.

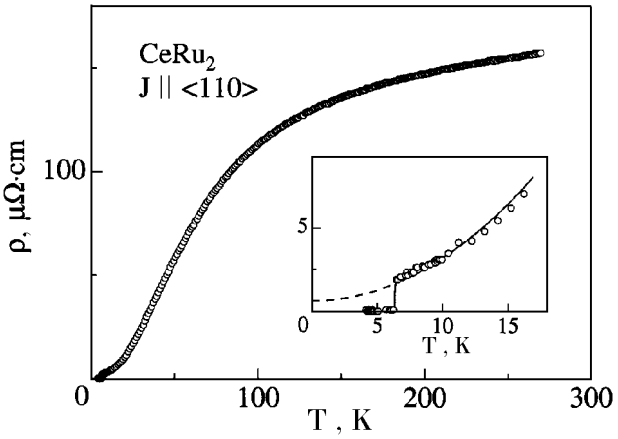

Fig. 12. Electrical resistivity of $CeRu_2$.

Table 1

Superconducting properties of $CeRu_2$, URu_2Si_2 and UPd_2Al_3

		T_c , K	H_{c2} , kOe	H_c , kOe	H_{c1} , kOe	ξ, Å	λ, Å	κ
$CeRu_2$		6.2	52.3	1.49	0.175	79.3	1980	25
URu_2Si_2	$H \parallel [100]$	1.3–1.5	130	0.8	0.033	64	4600	70
	$H \parallel [001]$		30					
UPd_2Al_3	$H \parallel [0001]$	2	37	0.49	0.1	85	4000	47
	$H \parallel [11\bar{2}0]$		32					

Figure 13,*a* shows the dHvA oscillation for the field along ⟨111⟩ at 0.47 K. The dHvA oscillation is observed in both the normal and superconducting mixed states, although it is not observed near H_{c2} of about 50 kOe because of the so-called peak effect [36]. The fast Fourier transform (FFT) spectra in Fig. 13,*b* indicate that for two branches, denoted by $\varepsilon_{1,2,3}$ and δ_1 , the detected dHvA frequencies are the same between the normal and mixed states. The similar dHvA oscillations are obtained for any field

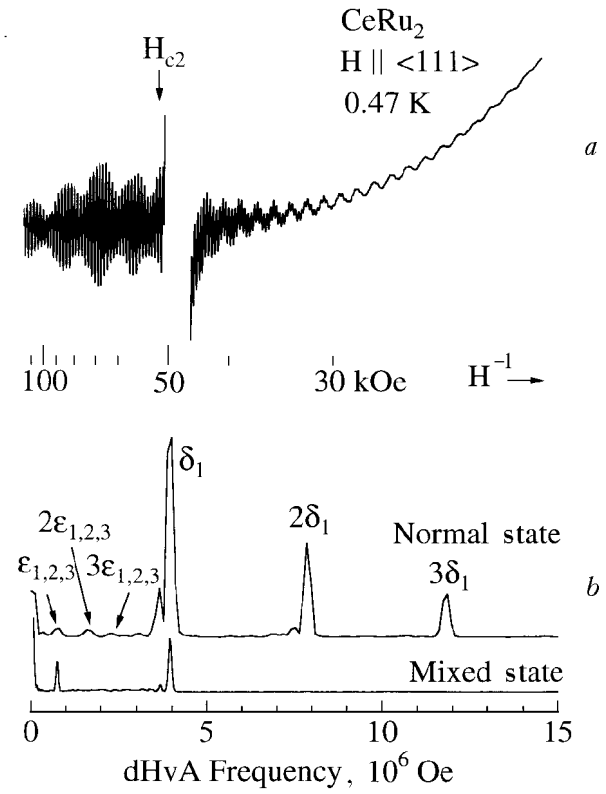

Fig. 13. Typical dHvA oscillation of $CeRu_2$ (*a*) and the corresponding FFT spectra in both the normal and superconducting mixed states (*b*).

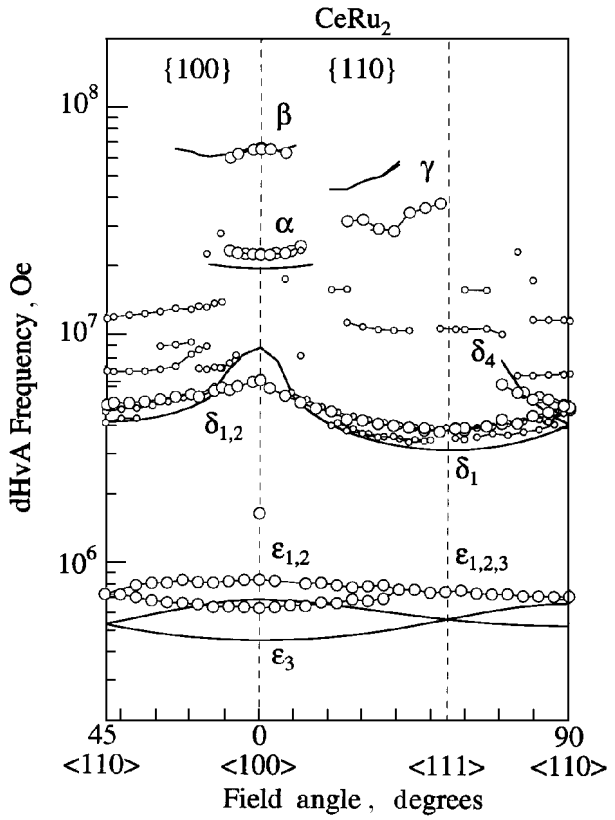

Fig. 14. Angular dependence of dHvA branches in $CeRu_2$. The data shown with large circles possess large magnitudes in FFT spectra, while those shown with small circles indicate small ones. Thin solid lines are guidelines, while thick solid lines are the result of band calculations.

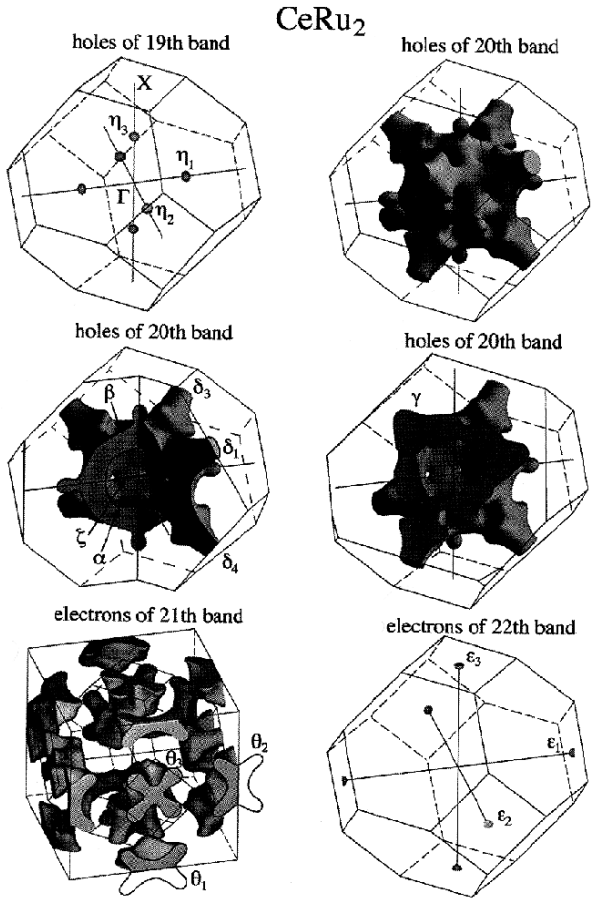

Fig. 15. Fermi surfaces of 19th band-hole, 20th band-hole, 21st band-electron and 22nd band-electron in $CeRu_2$.

direction. For example, branch α is observed for the field along ⟨100⟩ in both the normal and mixed states.

Figure 14 shows the angular dependence of the dHvA frequency. The data denoted by large circles indicate clear and large signals, while those denoted by small circles do not indicate harmonics or sums and differences of the fundamental dHvA frequencies but signals of small amplitudes. Thin solid lines are guidelines, while thick solid lines show the corresponding result of band calculations. Figure 15 indicates the Fermi surfaces based on the relativistic linear augmented-plane-wave (RLAPW) calculations under the assumption that $4f$ electrons are itinerant. The dHvA data are in good agreement with the result of band calculations.

Next we have determined the cyclotron mass m_c^* from the temperature dependence of the dHvA am-

Table 2

The de Haas-van Alphen frequency and the corresponding cyclotron mass for the typical field direction in $CeRu_2$. The angle of 42° means the field direction tilted by 42° from ⟨100⟩ to ⟨110⟩ in {110}

	Experimental					Theoretical		
	Branch	F, 10^6 Oe	m_c^*, m_0	T_D, K	l, Å	Band	F, 10^6 Oe	m_b, m_0
$H \parallel \langle 100 \rangle$	β	65.8	7.61			20	64.6	0.22
	α	22.6	2.64	0.57	2450	20	19.7	0.76
	$\delta_{1,2}$	6.38	4.39			20	6.38	1.97
	$\varepsilon_{1,2}$	0.84	0.71			22	0.69	0.31
	ε_3	0.63	0.55			22	0.46	0.20
⟨111⟩	δ_1	3.97	1.56	0.5	1980	20	3.16	0.50
	$\varepsilon_{1,2,3}$	0.75	0.61	0.45	2450	22	0.57	0.26
⟨110⟩	$\delta_{1,2}$	4.60	1.90			20	4.13	0.68
42°	γ	36.8	8.20			20	58.5	4.30

plitude, namely from a so-called mass plot. We show in Table 2 the dHvA frequency and the corresponding mass for the typical field directions in the normal state.

We have also determined the cyclotron mass by six cycles of the dHvA oscillation in the mixed state. The field dependence of the cyclotron mass for branches α, δ_1 and $\varepsilon_{1,2,3}$ is shown in Fig. 16,*a*. The cyclotron mass gradually decreases below H_{c2}. It is interesting that the ratio of the cyclotron mass in the mixed state $\tilde{m}_c^*$ to that in the normal state m_c^* shows a similar field dependence in the mixed state for three branches, as shown in Fig. 16,*b*. Here the solid line indicates the theoretical curve of Eq. (13), where $2\Delta(T=0)/k_BT_c = 3.7$ and Fermi velocity $v_F = 9.1 \cdot 10^6$ cm/s are used in calculations for the branch $\varepsilon_{1,2,3}$. The value of $2\Delta(T=0)/k_BT_c = 3.7$ was obtained from the specific heat measurement for the same sample [35]. The theoretical curve is highly different from the experimental data.

A similar field dependence is also observed for the Dingle temperature T_D. T_D in the normal state has been determined from the field dependence of the dHvA amplitude at constant temperatures of 0.5 K and 30 mK, namely, from a so-called Dingle plot. Figure 17,*a* shows the field dependence of the Dingle temperature for three branches. The difference $\Delta T_D = \tilde{T}_D - T_D$ between the Dingle temperature $\tilde{T}_D$ in the mixed state and the Dingle temperature T_D in the normal state is also shown in Fig. 17,*b*. Here we note that the «Dingle plot» to determine T_D is not valid for the present dHvA oscillation in the mixed state because both m_c^* and T_D depend on the field in the mixed state. We have determined the Dingle temperature so as to fit the dHvA amplitude following the Lifshitz-Kosevich formula under the assumption that the cyclotron mass in the mixed state decreases linearly with decreasing the field as shown in Fig. 16,*a*. As shown in Fig. 17,*b*, ΔT_D increases with decreasing the field below H_{c2}.

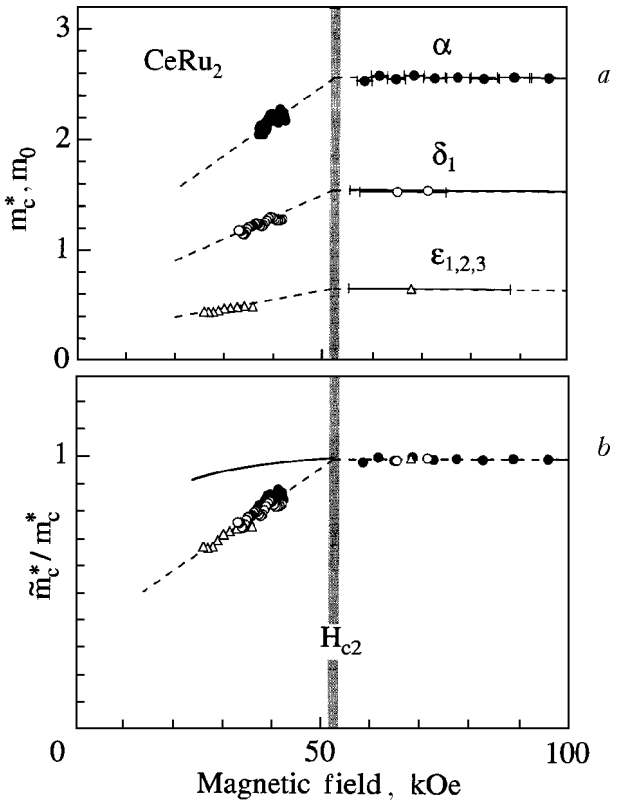

Fig. 16. Field dependence of the cyclotron mass for three branches; m_c^* (*a*) and $\tilde{m}_c^*/m_c^*$ (*b*) in $CeRu_2$.

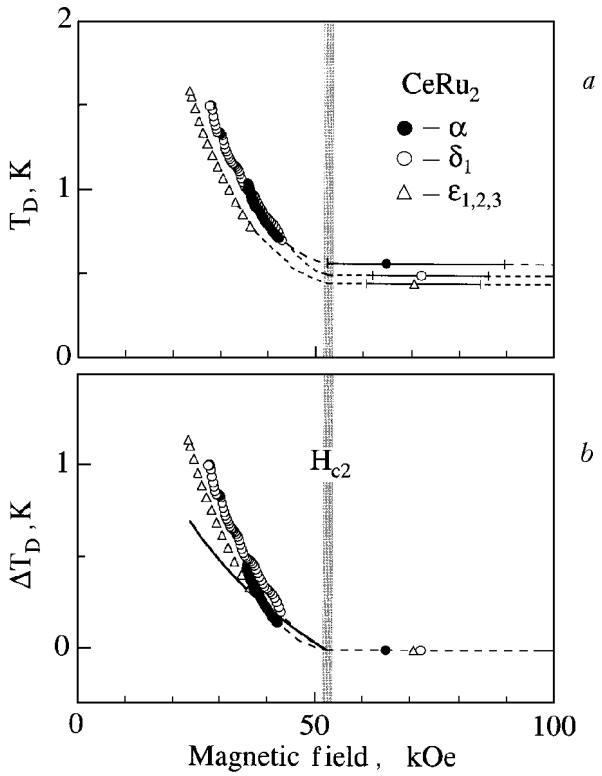

Fig. 17. Field dependence of the Dingle temperature for three branches; T_D (*a*) and ΔT_D (*b*) in $CeRu_2$.

We have measured the sample dependence of the Dingle temperature to study the additional damping term in the mixed state for branch $\varepsilon_{1,2,3}$, as shown in Fig. 18. Five samples of different quality were used in the experiments. The Dingle temperature in the mixed state $\tilde{T}_D$ depended on the magnetic field. A following simple relation holds between the Dingle temperature in the mixed state $\tilde{T}_D$ and that in the normal T_D ; $\tilde{T}_D = T_D + \Delta T_D$, where ΔT_D is an additional Dingle temperature in the mixed state. Namely, the value of ΔT_D shows approximately the similar field dependence for five samples. The solid lines in Figs. 17,*b* and 18,*b* represent the theoretical result of Eq. (7) for branch $\varepsilon_{1,2,3}$. The theoretical

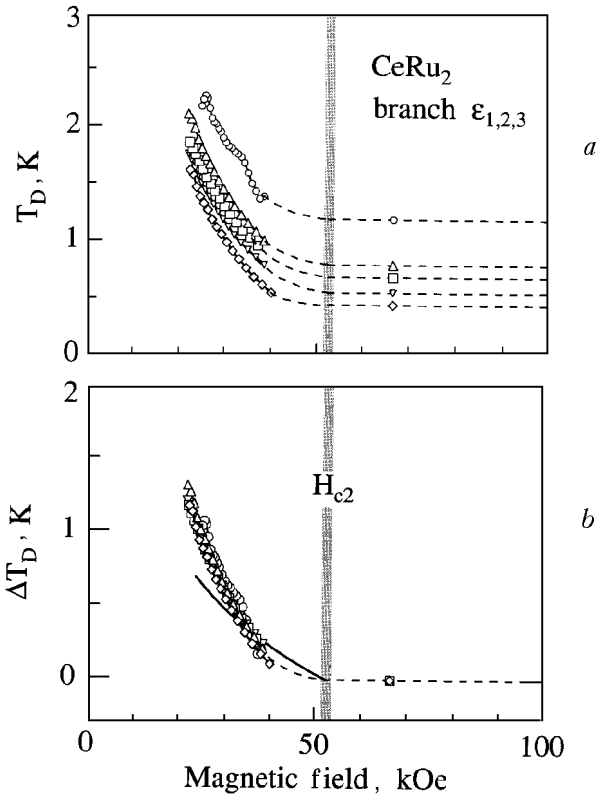

Fig. 18. Field dependence of the Dingle temperature for branch $\varepsilon_{1,2,3}$ in five different samples of $CeRu_2$; T_D (*a*) and ΔT_D (*b*).

curve is approximately consistent with the experimental one.

3.2. URu_2Si_2

Among the uranium intermetallic compounds, URu_2Si_2 and UPd_2Al_3 are fascinating magnetic superconductors. They are classified as the heavy fermion compounds. Qusiparticles with a heavy mass of 10–100 m_0 are of an *f*-electron character, condensing into Cooper pairs. Superconductivity is realized in the antiferromagnetic state. The ordered state in URu_2Si_2 is, however, anomalous because of an unusually small moment of 0.03 μ_B/U [37]. On the other hand, UPd_2Al_3 has a relatively large moment of 0.85 μ_B/U [38].

In the Ce-based heavy fermion compound such as $CeRu_2Si_2$, the magnetic susceptibility χ increases with decreasing the temperature, following the Curie-Weiss law with the effective moment of Ce^{3+}, and possesses a maximum at a characteristic temperature $T_{\chi\,\max}$. The magnetic susceptibility becomes thus constant at lower temperatures, indicating enhanced Pauli paramagnetism, as shown in Fig. 19. This large susceptibility is correlated with the large mass. The temperature $T_{\chi\,\max}$ approximately corresponds to the Kondo temperature T_K .

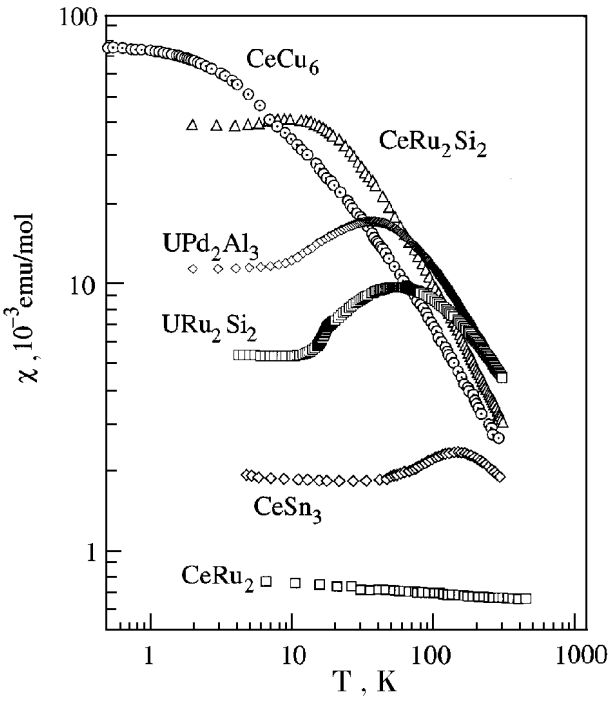

Fig. 19. Temperature dependence of the magnetic susceptibility for Ce and U compounds.

The similar behavior is observed in URu_2Si_2 and UPd_2Al_3 . The susceptibility for the field along [001] in URu_2Si_2 and for [11$\bar{2}$0] in UPd_2Al_3 increases with decreasing the temperature, following the Curie-Weiss law, and has a maximum at $T_{\chi\,\max} \simeq 55$ K in URu_2Si_2 and 35 K in UPd_2Al_3 . At lower temperatures both compounds order antiferromagnetically.

Figure 20 shows the tetragonal crystal structure of URu_2Si_2 , where arrows indicate the directions

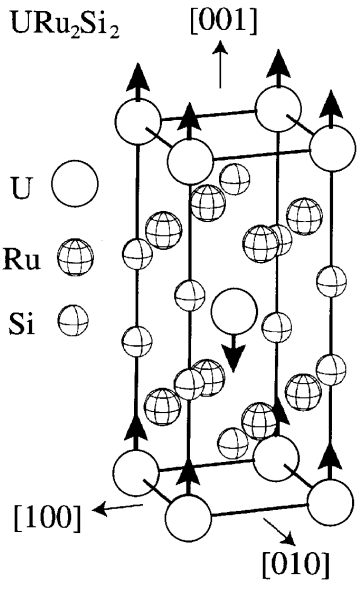

Fig. 20. Crystal structure of URu_2Si_2 . Arrows show the directions of the antiferromagnetic moments.

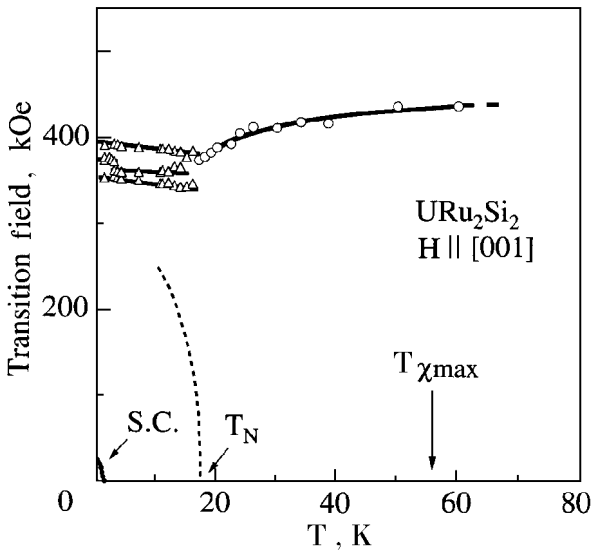

Fig. 21. Phase diagram of URu_2Si_2 .

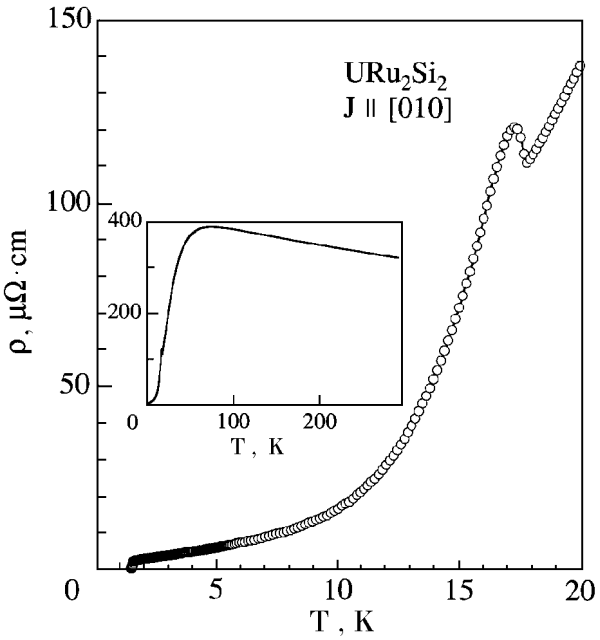

Fig. 22. Temperature dependence of the electrical resistivity in URu_2Si_2 . The inset shows the overall behavior of the resistivity.

of the antiferromagnetic moments. The phase diagram is shown in Fig. 21. The metamagnetic transition occurs at about 400 kOe. This transition with three steps is sharp when observed below the Néel temperature T_N = 17.5 K, and become broad above T_N , changing into one step in the metamagnetic transition. The transition field slightly increases with increasing the temperature [39]. A temperature dependence of the Néel temperature in the magnetic field is also shown by a dotted line in Fig. 21 [40]. This phase boundary is not directly related to the observed metamagnetic transition, although the metamagnetic transition itself is closely related to the antiferromagnetic ordering. In the phase diagram, S.C. denotes the superconducting state.

Transport, thermal and magnetic data indicate that this magnetic order below 17.5 K opens a gap on a large part of the Fermi surface. The corresponding electronic specific heat coefficient γ is changed from 110 to 64 mJ/(K^2·mol) through this transition, indicating that about 40% of the Fermi surface is removed after this transition [41]. Superconductivity occurs below the critical temperature T_c = 1.4 K in the antiferromagnetic state. $H_{c2}(0)$ at 0 K is highly anisotropic, being about 130 kOe for the field along [100] (a-axis) and about 30 kOe for [001] (c-axis) [42,43]. Below T_c the specific heat and the spin-lattice relaxation rate follow T^2- and T^3-dependences, respectively [43,44]. These results claim a line node in the superconducting energy gap. Superconducting properties are summarized in Table 1 [43,45].

A single crystal of URu_2Si_2 was grown by the Czochralski method in a tetra-arc furnace. The starting material of U was purified by the electro-transport method in high vacuum of 10^{-10} Torr. See the details in Ref. 46. An ingot of 3–4 mm in diameter and 80 mm in length was purified again by the electro-transport method in high vacuum of $1{\cdot}10^{-11}$ Torr, for one week.

First we show in Fig. 22 the temperature dependence of the electrical resistivity in the current J along the [010] direction. The resistivity has a peak at about 17 K, which corresponds to the Néel temperature, and decreases steeply with decreasing the temperature. The overall behavior of the temperature dependence of the resistivity is shown in an inset of Fig. 22. The resistivity increases with decreasing the temperature and shows a characteristic peak around 70 K, similar as that in heavy fermion compounds $CeCu_2Si_2$ and $CeCu_6$ [47].

As shown in Fig. 22, the resistivity become zero below 1.5 K. The residual resistivity extrapolated to 0 K, ρ_0 and the residual resistivity ratio (RRR), ρ_{RT}/ρ_0 are 1.27 μΩ·cm and 255, respectively. This sample is, as far as we know, the best sample.

Next we have determined the upper critical field H_{c2} from the electrical resistivity data in the magnetic field. Figure 23 shows the angular dependence of the upper critical field at 40 mK. The solid line is a theoretical curve based on the formula [43]:

$$H_{c2}(\theta) = \frac{H_{c2}(H \parallel [100])}{(\cos^2\theta + \kappa^2 \sin^2\theta)^{1/2}}\,, \qquad (15)$$

where H_{c2} $(H \parallel [100])$ is 130 kOe and $\kappa\,[= H_{c2}(H \parallel [100])/H_{c2}\,(H \parallel [001])] = 4.5$. H_{c2} is

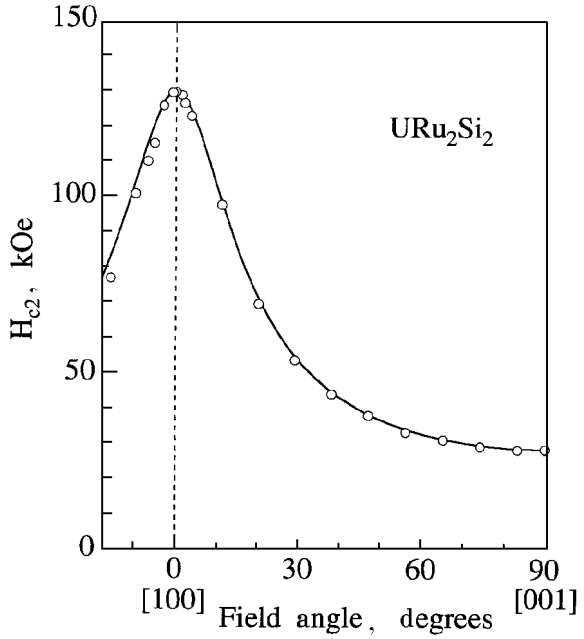

Fig. 23. Angular dependence of H_{c2} at 40 mK in URu_2Si_2 .

highly anisotropic, which is due to the paramagnetic effect, reflecting the anisotropic magnetic susceptibility. We also show in Fig. 24 the temperature dependence of H_{c2} for fields along [100] and [001]. These data are almost the same as the previous results [43].

We show in Fig. 25 the typical dHvA oscillation in both the normal and mixed states and the corresponding FFT spectra for a tilt angle $\theta = 8.1°$ in the field range from 40 to 150 kOe at 35 mK. The magnetic field direction was tilted by θ from [100] to [001]. One dHvA branch named α is clearly

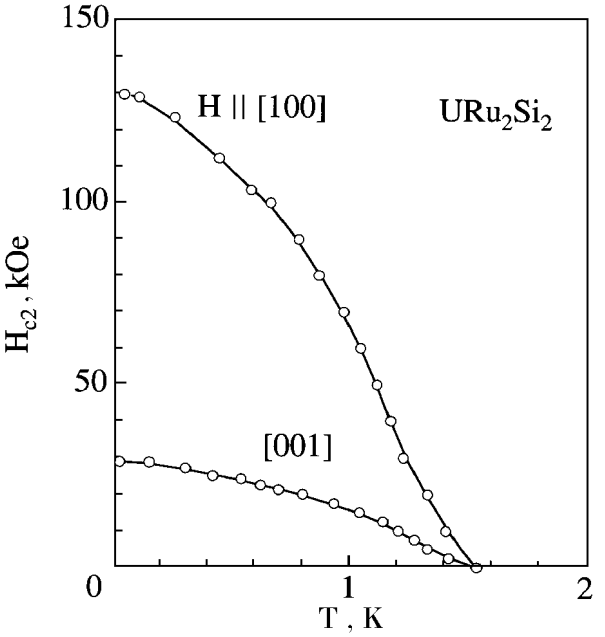

Fig. 24. Temperature dependence of H_{c2} for fields along [100] and [001] in URu_2Si_2 .

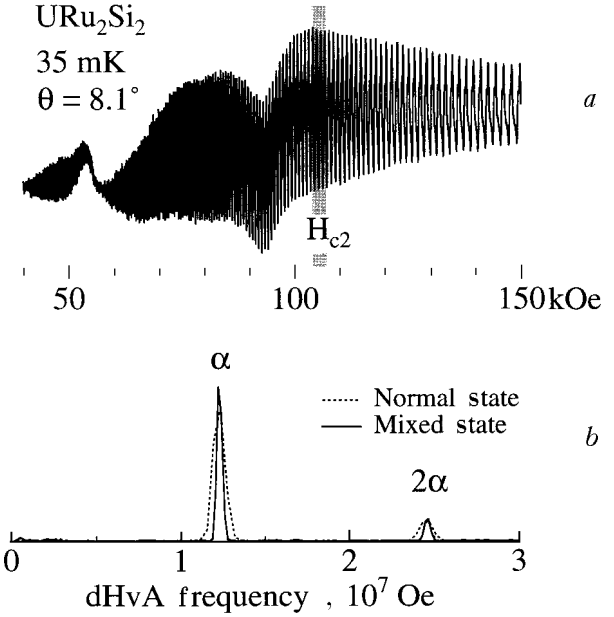

Fig. 25. DHvA oscillation and the corresponding FFT spectrum for a tilt angle $\theta = 8.1°$ in URu_2Si_2 .

observed in both the normal and mixed states. In other directions, another branches named β and γ are detected in the normal state, although their amplitudes are small.

Figure 26 shows the angular dependence of the dHvA frequency F. Branch α is almost constant as a function of the field tilt angle θ, indicating that the Fermi surface is spherical. In the (001) plane,

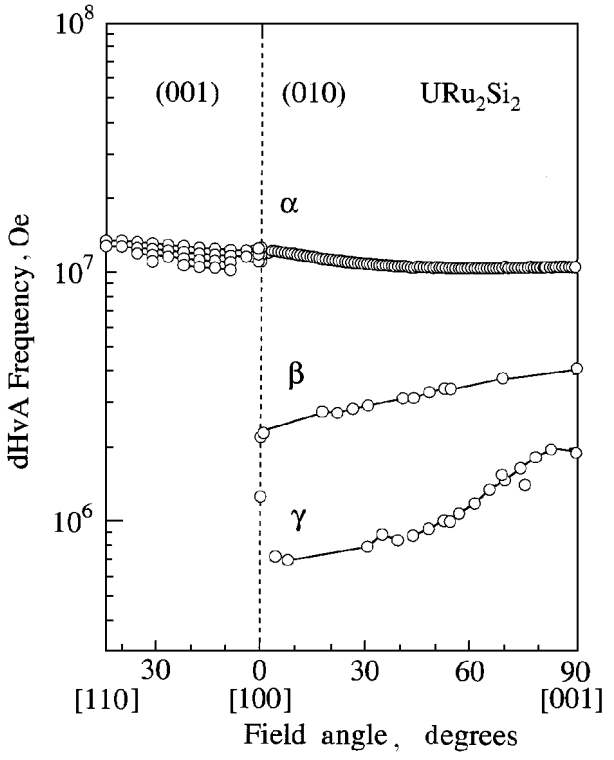

Fig. 26. Angular dependence of the dHvA frequency in URu_2Si_2 .

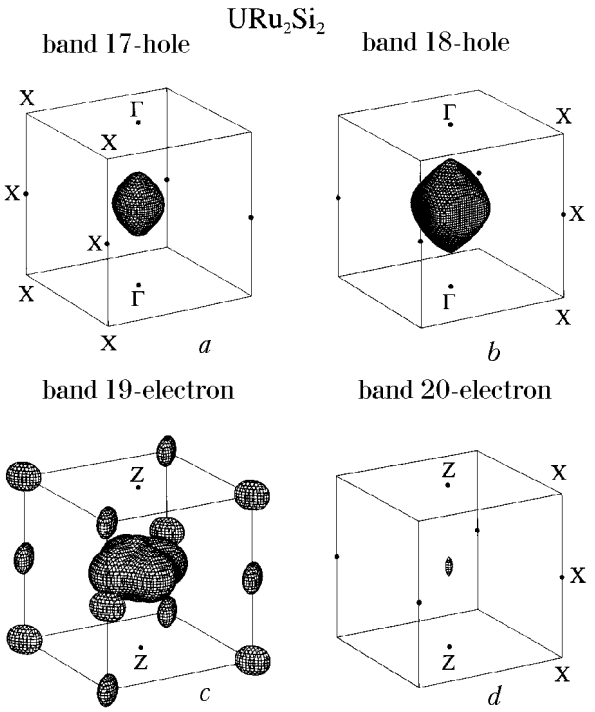

Fig. 27. Fermi surfaces for URu_2Si_2 in the paramagnetic state. The band 17-hole centered at the Z point (a), the band 18-hole at the Z point (b), the band 19-electrons at the Γ and X points (c) and the band 20-electron at the Γ point (d).

branch α is four-fold split. The reason of this splitting is not clear. The Fermi surface might be corrugated, possessing maxima and minima in cross-section.

Branches β and γ are not observed in the whole field angle. According to the previous report by Keller et al. [48], similar branches have been observed. Branches β and γ were also observed by Keller et al. at some field angles in the (001) and (010) planes. From these dHvA and also the magnetoresistance results [11], we conclude that three branches represent closed Fermi surfaces.

When we compare the dHvA result with the result of band calculations in an itinerant 5f-band model shown in Fig. 27, branches α, β and γ might correspond to the band 17-hole, 19-electron centered at X and 20-electron Fermi surfaces, respectively, in magnitude, although γ is different from the theoretical one in the angular dependence. These Fermi surfaces are small in volume. Much larger Fermi surfaces of bands 18-hole and 19-electron have not been observed experimentally. If we assume that these larger Fermi surfaces disappear completely below the ordering temperature, this change of the Fermi surface is inconsistent with the reduction of the electronic specific heat coefficient [41]. There should exist other remaining Fermi surfaces not observed in our experiment because URu_2Si_2 is a compensated metal with equal numbers of electrons and holes from the result of the magnetoresistance, and then the hole Fermi surface of branch α does not compensate with the electron Fermi surfaces of branches β and γ in volume.

Next, we have determined the cyclotron mass from the temperature dependence of the dHvA amplitude, and the Dingle temperature from the field dependence of the dHvA amplitude for the field along [001]. All branches are heavy. The cyclotron masses are 13 m_0 for branch α, 25 m_0 for β and 8.2 m_0 for γ. It is surprising that a small Fermi surface of branch β possesses such a large cyclotron mass. The Dingle temperature is small, 0.035 K for branch α, 0.045 K for β and 0.11 K for γ, indicating a high-quality sample. We have determined the mean free path l from the relation of $S_F = \pi k_F^2$, $\hbar k_F = m_c^* v_F$ and $l = v_F \tau$, where v_F is Fermi velocity and k_F is half of the caliper dimension of the Fermi surface. The l-value is large, 5500 Å for branch α, 1400 Å for β and 1200 Å for γ. These values are by one order larger than the coherence length ξ, indicating that superconductivity is close to the pure limit. These Fermi surface properties are summarized in Table 3.

We show in Fig. 28,a the typical dHvA oscillation for the field along [001]. H_{c2} is about 29 kOe. The dHvA oscillation named α is observed in the

Table 3

The de Haas-van Alphen frequency F, the cyclotron effective mass m_c^*, the band mass m_b, the Dingle temperature T_D and the mean free path l in URu_2Si_2

Experimental						Theoretical	
$H \parallel [001]$	F, 10^6 Oe	m_c^*, m_0	T_D, K	l, Å		F, 10^6 Oe	m_b, m_0
α	10.5	13	0.035	5500	band 17 (Z)	18.5	1.62
					band 18 (Z)	36.8	2.72
					band 19 (Γ)	62.9	8.02
β	4.2	25	0.045	1400	band 19 (X)	4.6	3.20
γ	1.9	8.2	0.11	1200	band 20 (Γ)	0.3	0.25

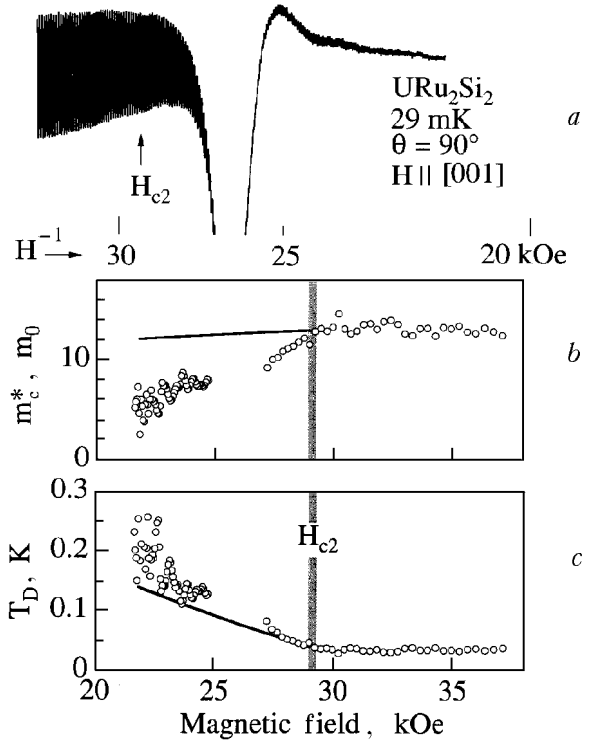

Fig. 28. DHvA oscillation at 29 mK for [001] (*a*), field dependences of the cyclotron mass (*b*) and the Dingle temperature (*c*) in URu_2Si_2 .

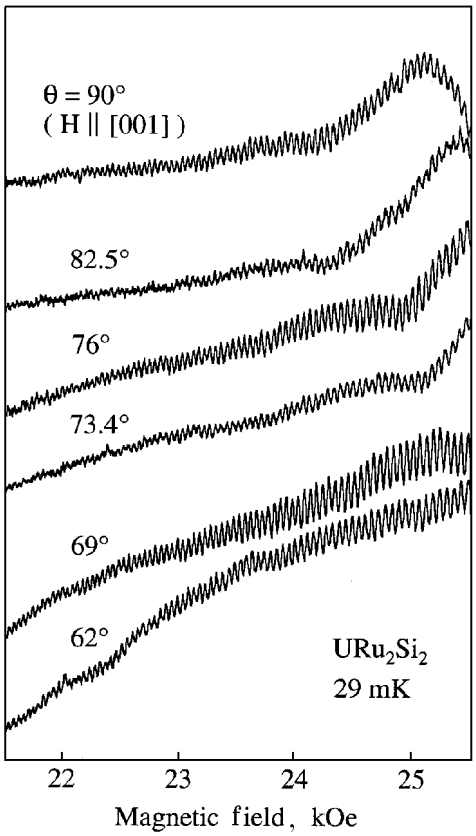

Fig. 29. DHvA oscillations for several tilt angles in the (010) plane for URu_2Si_2 .

mixed state down to about 20 kOe. Figure 28,*b* shows the field dependence of the cyclotron mass. We determined the mass from the temperature dependence of the dHvA amplitude over seven cycles of the oscillation. The cyclotron mass is constant above H_{c2} , but decreases gradually with decreasing the field below H_{c2} . The mass is not correctly determined in the field range from 25 to 28 kOe because this is a region of the so-called peak effect.

A similar field dependence is also observed for the Dingle temperature T_D , as shown in Fig. 28,*c*. T_D was determined directly from the dHvA amplitude by using the mass in Fig. 28,*b*. The Dingle temperature in the mixed state increases with decreasing field below H_{c2} . Solid lines in Fig. 28,*b* and *c* are theoretical curves of Eqs. (13) and (7) for branch α, where a BCS relation of $2\Delta/k_BT_c = 3.54$ and $v_F = 1.6 \cdot 10^6$ cm/s were used in calculations. The theoretical curve for T_D is approximately consistent with the experimental one, while the theoretical field dependence of the mass is highly different from the experimental one, as in $CeRu_2$.

An interesting point in URu_2Si_2 is an anisotropic energy gap because the existence of the line node is clear from the specific heat [43] and the nuclear spin-lattice relaxation rate [44] experiments. It was discussed theoretically that the superconducting gap disappears as a line node on the Fermi surface, for momenta perpendicular to the antiferromagnetic wave vector parallel to the [001] direction, as shown in Fig. 10,*a* and *b* [49]. We have tried to determine the position of the line node on the Fermi surface via the dHvA experiment.

Figure 29 shows the dHvA oscillation for several field directions. The tilt angle θ is the field angle from [100] to [001], as defined above. No appreciable change of the dHvA oscillation has been found for any field, when the field is tilted from [001] to [100].

In Fig. 30 the angular dependences of the dHvA amplitudes in both the normal and mixed states are represented by circles and squares, respectively. Effective fields are 46.9 kOe in the normal state and 23.7 kOe ($\simeq 0.8H_{c2}$) in the mixed state. The amplitude reduction for several field angles is due to the zero spin-splitting. This is reflected even in the mixed state. This result shows clearly that it is difficult to distinguish experimentally the line node in the anisotropic energy gap from the gapless state based on the pair-breaking in the magnetic field. The former effect schematically shown in Fig. 10,*a* and *b* is compared to the latter one in Fig. 8,*c*. If the dHvA oscillation is found in the mixed state far

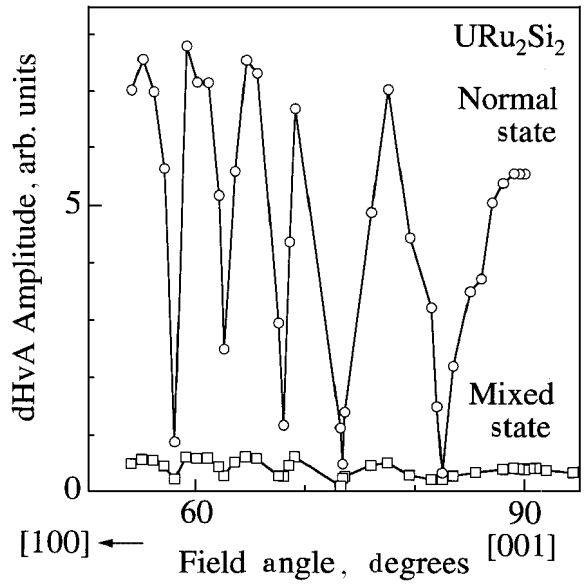

Fig. 30. Angular dependence of the dHvA amplitude in both the normal and mixed states for branch α in URu_2Si_2 .

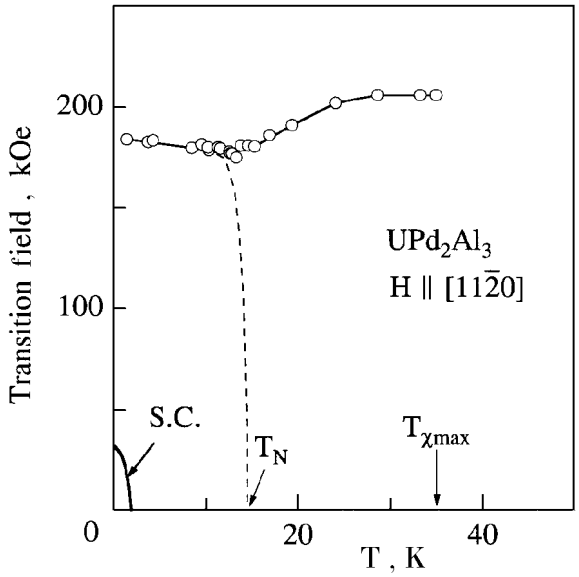

Fig. 32. Phase diagram of UPd_2Al_3 .

below H_{c2} , the former should be distinguished from the latter.

The dHvA oscillation is observed in fields down to 30–40 kOe in the (001) plane. No appreciable change of the dHvA oscillation for any field direction in the (001) plane was found. This result also implies that a line node, as shown in Fig. 10,*c*, does not exist and/or it is difficult to distinguish experimentally the line node with the gapless state, as in the (010) plane.

3.3. UPd_2Al_3

UPd_2Al_3 with the hexagonal structure is also a fascinating magnetic superconductor [50]. Superconductivity with the transition temperature $T_c \simeq$ $\simeq$ 2 K is realized in the antiferromagnetic state with the Néel temperature T_N = 14 K. Neutron scattering measurements revealed that the magnetic moments of 0.85 μ_B/U are ferromagnetically oriented along the [11$\bar{2}$0] direction but are coupled antiferromagnetically along the [0001] direction with the wave vector Q = (0, 0, 0.5) [38], as shown in Fig. 31. Superconducting properties are summarized in Table 1.

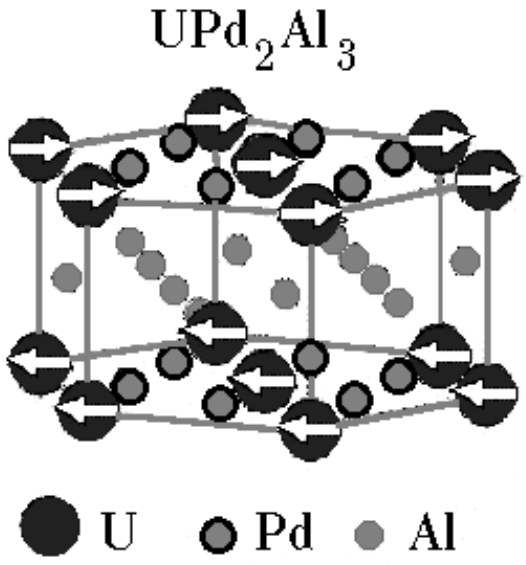

Fig. 31. Crystal structure of UPd_2Al_3 . Arrows indicate the directions of the antiferromagnetic moments.

The high-field magnetization indicates a sharp metamagnetic transition at about 180 kOe below T_N = 14 K. It becomes, however, broad above T_N . This metamagnetic transition occurs for the field parallel to the basal plane, indicating a XY-type in character, which is compared to an Ising type along [001] in URu_2Si_2 .

Figure 32 shows the phase diagram. The metamagnetic transition is found above T_N , up to the characteristic temperature, $T_{\chi\,\max}$ = 35 K. This means that this transition is not related to the antiferromagnetic ordering but to a change of the 5*f*-electron character as in URu_2Si_2 . We note that the ordered state, which is shown by a dotted line in Fig. 32, is closely related to the sharpness of the metamagnetic transition. In the phase diagram, S.C. denotes the superconducting state.

Figure 33 shows the temperature dependence of the electrical resistivity ρ. Overall features are the same as the previously reported ones [50]. As seen in an inset of Fig. 33, we observed a Kondo-like logarithmic-temperature dependence from room temperature to about 100 K, a sharp decrease below T_N = 14 K and finally a superconducting transition

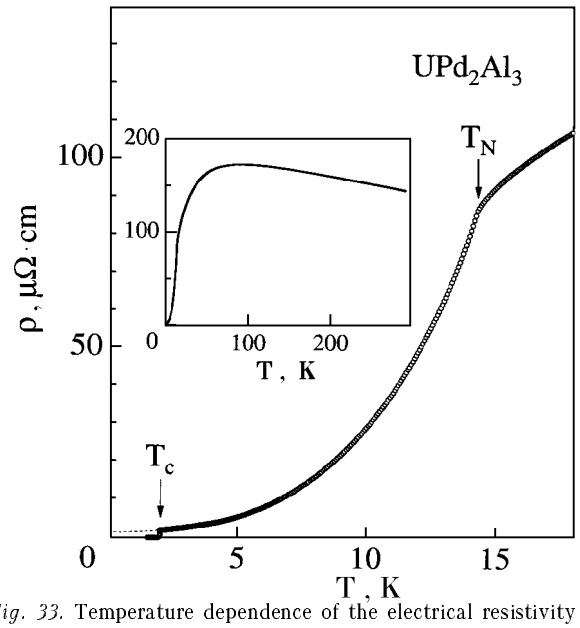

Fig. 33. Temperature dependence of the electrical resistivity of UPd_2Al_3 . The inset shows the resistivity from room temperature to 1.5 K.

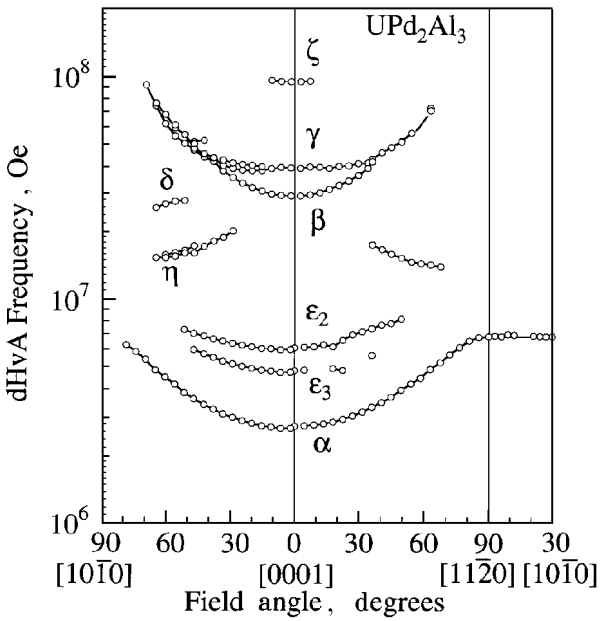

Fig. 35. Angular dependence of the dHvA frequency in UPd_2Al_3 .

at $T_c = 1.9$ K. The residual resistivity extrapolated to 0 K, ρ_0 , as shown by a dotted line in Fig. 33, and the residual resistivity ratio ρ_{RT}/ρ_0 are

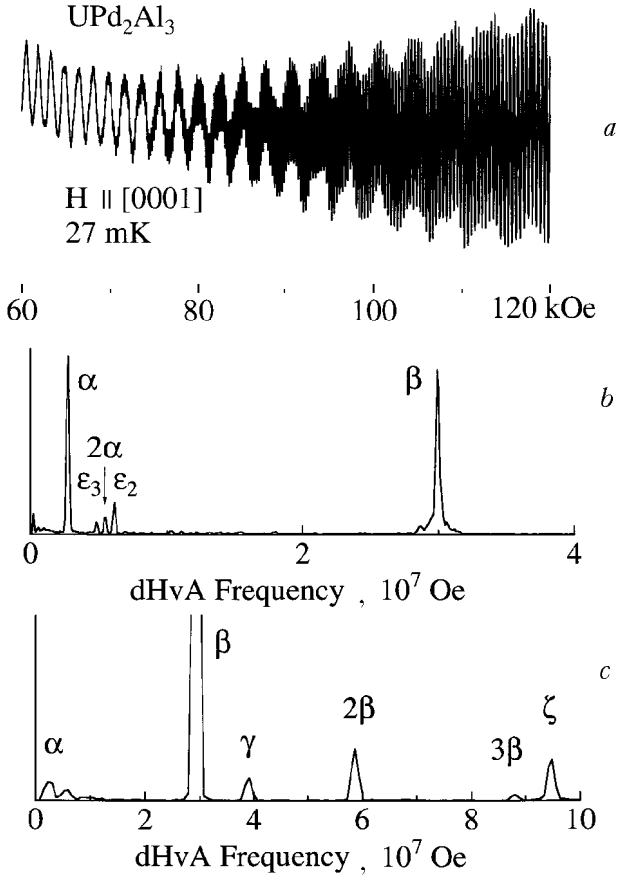

Fig. 34. DHvA oscillation and the corresponding FFT spectra for the field along [0001] in UPd_2Al_3 .

1.40 μΩ·cm and 104, respectively. These are the best values as far as we know. The present single crystal was grown by the Czochralski method in a tetra-arc furnace, as described in Ref. 51 in detail.

Figure 34 shows the typical dHvA oscillation and the corresponding FFT spectrum for the magnetic field along the [0001] direction. Magnetic fields used in the FFT spectra are in the ranges from 60 to 120 kOe in Fig. 34,*b* and from 138 to 169 kOe in Fig. 34,*c*. Figure 35 shows the angular dependence of the dHvA frequency.

Almost all of the branches labeled α, β, γ, δ and ε_3 are the same as the previous dHvA results obtained by Inada et al. [52]. According to the previous result of band calculations [53,54], where 5*f* electrons were treated as itinerant electrons and brought about the antiferromagnetic moment of

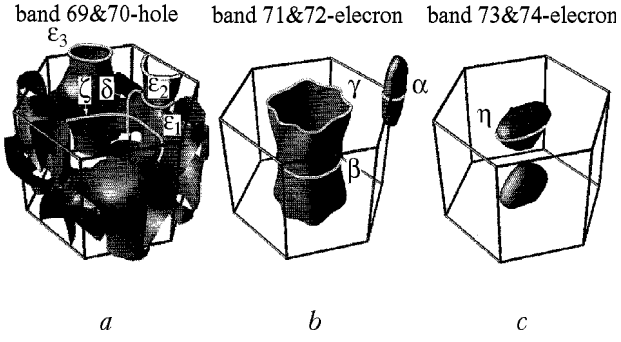

Fig. 36. Band 69&70-hole (*a*), band 71&72-electron (*b*) and band 73&74-electron Fermi surfaces (*c*) of UPd_2Al_3 , cited from Ref. 54.

Table 4

The de Haas-van Alphen frequency F, the cyclotron effective mass m_c^*, the Dingle temperature T_D and the mean free path l in UPd_2Al_3. The theoretical frequency in the paramagnetic state is cited form Ref. 53

Experimental					Theoretical	
$H \parallel [0001]$	F, 10^7 Oe	m_c^*, m_0	T_D, K	l, Å		F, 10^7 Oe
ζ	9.45	65	0.10	1190	band 69&70 (Γ)	8.87
γ	4.06	33	0.28	540	band 71&72 (A)	3.82
β	3.06	19	0.15	1550	band 71&72 (Γ)	3.07
ε_2	0.61				band 69&70 (L)	1.50
ε_3	0.48					
α	0.26	5.7	0.20	1200	band 71&72 (H)	0.30

0.85 μ_B/U, branches ε_2, ε_3, δ and ζ are due to a band 69&70-hole Fermi surface called «party hat», branches β and γ correspond to the maximum and minimum cross-sectional areas of a band 71&72-electron Fermi surface called «column», branch α is due to an ellipsoidal band 71&72-electron Fermi surface called «cigar» and branch η is due to a band 73&74-electron Fermi surface named «egg», as shown in Fig. 36. In the hexagonal symmetry, branches ε_2 and ε_3 have the same cross-section, but they have different cross-sections, reflecting the magnetic moment oriented along $[11\bar{2}0]$ [53,54].

We have determined the values of the cyclotron mass and the Dingle temperature, as shown in Table 4. These values are almost the same as the previous results [52]. We note that branch ζ has a large mass of 65 m_0. This is the largest mass in UPd_2Al_3. The masses in the range from 6 to 65 m_0 in Table 4 are consistent with a large γ-value of 145 mJ/(K^2·mol) [50]. T_D of 0.20 K is small, reflecting a high-quality sample. Therefore, the mean free path is longer than 1000 Å.

As shown in Fig. 37,*a*, the dHvA oscillation is clearly observed in both the normal and mixed states. The dHvA oscillation, which is observed up to the upper critical field H_{c2} (= 39 kOe) with decreasing field, is due to branch α. This branch is still seen in the mixed state at fields down to about 25 kOe. The dHvA oscillation is not observed in the field range from 39 to 31 kOe, which is due to the peak effect, as discussed before [51]. The dHvA frequency of $2.64 \cdot 10^6$ Oe for branch α is the same between the normal and mixed states. We have determined the cyclotron mass m_c^* from the temperature dependence of the dHvA amplitude over six cycles of the dHvA oscillation. As shown in Fig. 37,*b*, the mass decreases gradually with decreasing the field below H_{c2}. The cyclotron mass at 24 kOe (= $0.62H_{c2}$) is 3.8 m_0, which is compared to the mass of 5.6 m_0 in the normal state.

A similar field dependence is also observed for the Dingle temperature T_D, as shown in Fig. 37,*c*. The Dingle temperature in the mixed state increases steeply with decreasing field below H_{c2}. The solid line in Fig. 37,*c* is a theoretical curve of Eq. (7) for branch α, where the BCS relation of $2\Delta/k_BT_c = 3.54$ and Fermi velocity $v_F = 1.86 \cdot 10^6$ cm/s are used in calculations. The Dingle temperature in the mixed state in Fig. 37,*c* is slightly smaller than the theoretical curve. On the other hand, the cyclotron mass is reduced compared to the theoretical one, as shown in Fig. 37,*b*. The mass reduction was not found in other non-*f* compounds. It was found only for $CeRu_2$, URu_2Si_2 and now for UPd_2Al_3.

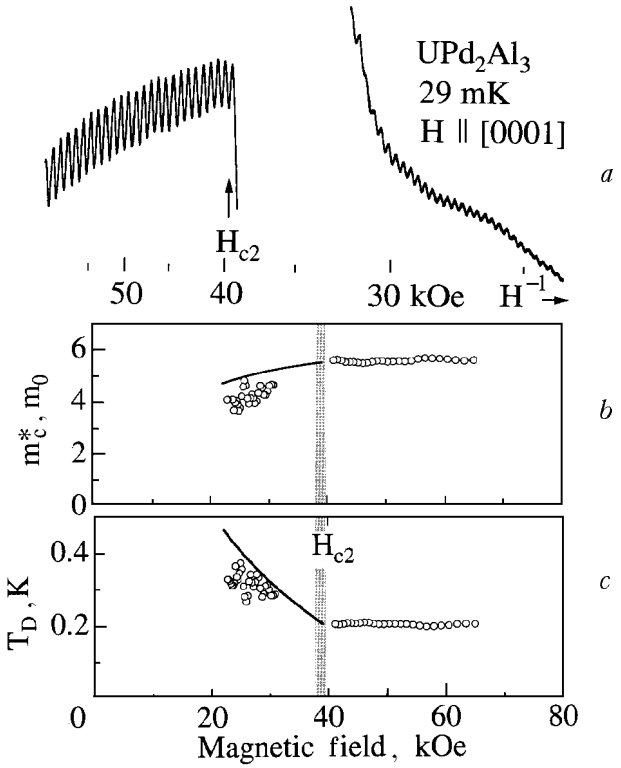

Fig. 37. DHvA oscillation at 29 mK for [0001] (*a*), field dependences of the cyclotron mass (*b*) and the Dingle temperature (*c*) in UPd_2Al_3.

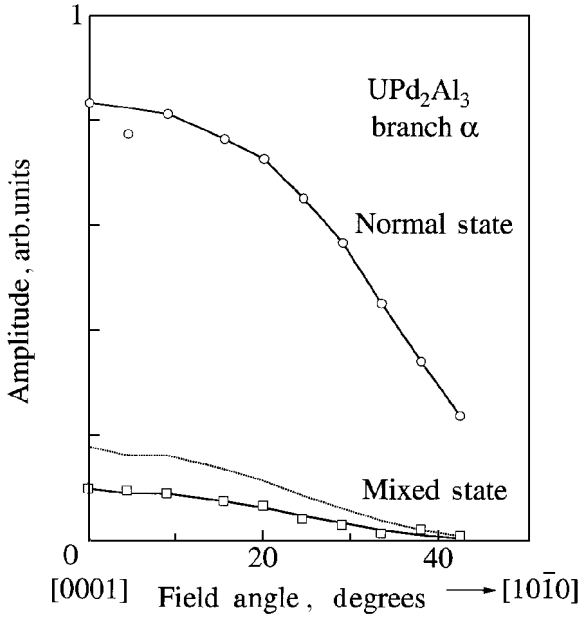

Fig. 38. Angular dependence of the dHvA amplitude in UPd_2Al_3.

As mentioned above, S_F is the extremal cross-sectional area of the Fermi surface by planes perpendicular to the field direction. If S_F corresponds to the maximum cross-section with the line node, it is not easy to distinguish the line node in the anisotropic energy gap from the gapless state in magnetic fields, as in URu_2Si_2. We have also studied the angular dependence of the dHvA oscillation, as shown in Fig. 38. Here, the field angle θ is a tilt angle from [0001] to [10$\bar{1}$0]. The angular dependence of the dHvA amplitude is also shown in both the normal and mixed states. The dHvA amplitudes were obtained from the FFT spectra in the field range from 55.5 to 62.5 kOe in the normal state and from 25.0 to 26.5 kOe in the mixed state. The Fermi surface of branch α is approximately of an ellipsoid of revolution, as shown in Fig. 36, following $S_F(\theta) = 6.94 \cdot 10^6/(\sin^2\theta + (2.6)^2\cos^2\theta)^{1/2}$ Oe. The cyclotron mass in the normal state also shows the same angular dependence; $m_c^*(\theta) = 14.3/(\sin^2\theta + (2.6)^2\cos^2\theta)^{1/2} m_0$.

On the other hand, the Dingle temperature in the normal state is nearly angle-independent up to $\theta = 30°$; $T_D = 0.21$ K. By using these data, we can calculate the dHvA amplitude at 25.7 kOe ($\simeq 0.65\ H_{c2}$) which is an effective field in the field range from 25.0 to 26.5 kOe. Thus, the dotted line in Fig. 38 is the curve obtained at 25.7 kOe under the assumption that values of the cyclotron mass and the Dingle temperature in the normal state are unchanged in the mixed state. The dHvA amplitude data at 25.7 kOe, shown by squares in Fig. 38, are reduced roughly by one half, compared to the dotted line. If we fit the result calculated for $\theta = 0°$ ($H \parallel [0001]$) to the dHvA amplitude for $\theta = 0°$ in the mixed state, the dotted line is changed into a thick solid line. This solid line is in good agreement with the dHvA data in the mixed state. This result implies that a line node in the anisotropic energy gap, shown in Fig. 10,*a* and *b*, does not exist and/or it is difficult to distinguish experimentally the line node in the anisotropic energy gap from the gapless state based on pair-breaking by applying a magnetic field. If the dHvA oscillation is found in the mixed state far below H_{c2}, the line node should be distinguished from the gapless state in fields. That is, the dHvA data are expected to deviate from the thick solid line or to reduce steeply with increasing the tilt angle.

4. Concluding remarks

We have succeeded in growing high-quality single crystals of $NbSe_2$, $CeRu_2$, URu_2Si_2 and UPd_2Al_3 and observed the dHvA oscillation in both the normal and superconducting mixed states. Our experimental results can be summarized as follows:

1) The dHvA oscillation, which is observed near H_{c2} in the normal state, is also observed in the mixed state.

2) The dHvA frequency in the normal state remains unchanged in the mixed state.

3) The cyclotron mass in the mixed state decreases in magnitude with decreasing the field. This is found only in the *f* electron system, not observed in $NbSe_2$ and the other non-*f* electron superconductors. This can not be explained by Maki's theory based on the density of states in magnetic fields after Brandt et al.

4) The corresponding Dingle temperature is enhanced with increasing the field below H_{c2}. This is approximately explained by the Maki's theory.

5) We searched for the anisotropic energy gap from the angular dependence of the dHvA oscillation in the mixed state. From the present result, it was difficult to distinguish the line node in the anisotropic gap from the gapless state based on the pair-breaking in magnetic fields.

We suppose that the origin of the mass reduction below H_{c2} is related to the correlation effect between the quasiparticles [55]. In heavy fermion compounds, the magnetic part of the specific heat is changed into the electronic specific heat at low temperatures. For example, the 4*f*-levels of the Ce ion are generally split into three doublets at high temperatures because the 4*f*-electrons in the Ce compounds are almost localized in nature, following

the Curie-Weiss law. At low temperatures, the magnetic entropy of the ground-state doublet in the 4*f*-levels or the magnetic specific heat C_m is changed into the electronic specific heat γT via the many-body Kondo effect as follows:

$$R \ln 2 = \int_0^{T_K} \frac{C_m}{T} dT , \qquad (16)$$

$$C_m = \gamma T . \qquad (17)$$

The γ-value can be obtained as

$$\gamma = \frac{R \ln 2}{T_K} \simeq \frac{10^4}{T_K} \ \mathrm{mJ/(K^2 \cdot mol)} . \qquad (18)$$

In fact, the γ-value in $CeCu_6$ is 1600 mJ/(K^2·mol) for T_K = 5 K [47,56].

The magnetic susceptibility in URu_2Si_2 and UPd_2Al_3 increases with decreasing the temperature, following the Curie-Weiss law, and has a maximum at the characteristic temperature $T_{\chi\,\max}$. $T_{\chi\,\max}$ for URu_2Si_2 and UPd_2Al_3 approximately corresponds to the Kondo temperature T_K for $CeRu_2Si_2$ and $CeCu_6$ where almost localized 4*f*-electrons become itinerant below T_K , forming the heavy fermion state with an extremely large γ-value.

All energy bands in $CeRu_2$, URu_2Si_2 and UPd_2Al_3 contain the *f*-electron component and have flat dispersion, bringing about relatively large band masses. Nevertheless, the cyclotron effective masses are considerably larger than the corresponding band masses, as shown in Table 2–4. The mass enhancement is not included in the conventional band calculations. It is caused by spin fluctuations, where the freedom of the charge transfer of the *f*-electrons appears in the form of the *f*-itinerant band, but the freedom of spin fluctuations of the same *f*-electrons reveals an unusual magnetic ordering, especially in URu_2Si_2 and enhances the effective mass as in the many-body effect for $CeCu_6$ and $CeRu_2Si_2$. In the mixed state, the number of quasiparticles, which are produced on the basis of the pair-breaking in the magnetic fields, decreases with decreasing the field below H_{c2} . This might influence the correlation effect between the quasiparticles, most likely bringing about the mass reduction below H_{c2} .

We are very grateful to K. Maki, S. Koh, K. Miyake and J. Kübler for a helpful discussion and to M. Hedo, H. Ohkuni, K. Sugiyama, R. Settai, T. Honma, Y. Haga, E. Yamamoto, M. Higuchi, H. Yamagami, S. Takahashi, T. Yanagisawa and A. Hasegawa for collaborated studies. This work was supported by the Grant-in-Aid for COE Research (10CE2004) of the Ministry of Education, Science, Sports and Culture.

1. Y. Ōnuki and A. Hasegawa, *Handbook on the Physics and Chemistry of Rare Earths*, Vol. 20, K. A. Gschneidner, Jr. and L. Eyring (eds.), Elsevier, Amsterdam (1995), p. 1.
2. H. Aoki, S. Uji, A. K. Albessard, and Y. Ōnuki, *Phys. Rev. Lett.* **71**, 2110 (1993).
3. L. Taillefer and G. G. Lonzarich, *Phys. Rev. Lett.* **60**, 1570 (1988).
4. N. Kimura, T. Komatsubara, D. Aoki, Y. Ōnuki, Y. Haga, E. Yamamoto, H. Aoki, and H. Harima, *J. Phys. Soc. Jpn.* **67**, 2185 (1998).
5. J. E. Graebner and M. Robbins, *Phys. Rev. Lett.* **36**, 422 (1976).
6. Y. Ōnuki, I. Umehara, T. Ebihara, N. Nagai, and K. Takita, *J. Phys. Soc. Jpn.* **61**, 692 (1992).
7. Y. Ōnuki, I. Umehara, T. Ebihara, A. K. Albessard, K. Satoh, K. Takita, H. Aoki, S. Uji, and T. Shimizu, *Physica* **B186–188**, 1050 (1993).
8. R. Corcoran, N. Harrison, C. J. Haworth, S. M. Hayden, P. Meeson, M. Springford, and P. J. van der Wel, *Physica* **B206–207**, 534 (1995).
9. M. Hedo, Y. Inada, T. Ishida, E. Yamamoto, Y. Haga, Y. Ōnuki, M. Higuchi, and A. Hasegawa, *J. Phys. Soc. Jpn.* **64**, 4535 (1995).
10. M. Hedo, Y. Inada, K. Sakurai, E. Yamamoto, Y. Haga, Y. Ōnuki, S. Takahashi, M. Higuchi, T. Maehira, and A. Hasegawa, *Philos. Mag.* **B77**, 975 (1998).
11. H. Ohkuni, T. Ishida, Y. Inada, Y. Haga, E. Yamamoto, Y. Ōnuki, and S. Takahashi, *J. Phys. Soc. Jpn.* **66**, 48 (1997).
12. Y. Haga, Y. Inada, K. Sakurai, Y. Tokiwa, E. Yamamoto, T. Honma, and Y. Ōnuki, *J. Phys. Soc. Jpn.* **68**, 339 (1999).
13. T. J. B. M. Janssen, C. Haworth, S. M. Hayden, P. Meeson, M. Springford, and A. Wasserman, *Phys. Rev.* **B57**, 11698 (1998).
14. T. Terashima, H. Takeya, S. Uji, K. Kadowaki, and H. Aoki, *Solid State Commun.* **96**, 459 (1995).
15. M. Heinecke and K. Winzer, *Z. Phys.* **B98**, 147 (1995).
16. G. Goll, M. Heinecke, A. G. M. Jansen, W. Joss, L. Nguyen, E. Steep, K. Winzer, and P. Wyder, *Phys. Rev.* **B53**, 8871 (1996).
17. C. Bergemann, S. R. Jullian, G. J. McMullan, B. K. Howard, G. G. Lonzarich, P. Lejay, J. P. Brison, and J. Flouquet, *Physica* **B230–232**, 348 (1997).
18. M. Sigrist and K. Ueda, *Rev. Mod. Phys.* **63**, 239 (1991).
19. N. Sato, N. Aso, G. H. Lander, B. Roessli, T. Komatsubara, and Y. Endoh, *J. Phys. Soc. Jpn.* **66**, 1884 (1997).
20. N. Metoki, Y. Haga, Y. Koike, and Y. Ōnuki, *Phys. Rev. Lett.* **80**, 5417 (1998).
21. M. Kyogaku, Y. Kitaoka, K. Asayama, C. Geibel, C. Schank, and F. Steglich, *J. Phys. Soc. Jpn.* **61**, 2660 (1992).
22. K. Matsuda, Y. Kohori, and T. Kohara, *Phys. Rev.* **B55**, 15223 (1997).
23. H. Tou, Y. Kitaoka, K. Asayama, N. Kimura, Y. Ōnuki, E. Yamamoto, and K. Maezawa, *Phys. Rev. Lett.* **77**, 1374 (1996); *Phys. Rev. Lett.* **80**, 3129 (1998).
24. K. Tenya, M. Ikeda, T. Sakakibara, E. Yamamoto, K. Maezawa, N. Kimura, R. Settai, and Y. Ōnuki, *Phys. Rev. Lett.* **77**, 3193 (1996).

25. K. Matsuda, Y. Kohori, and T. Kohara, *J. Phys. Soc. Jpn.* **65**, 679 (1996).
26. K. Maki, *Phys. Rev.* **B44**, 2861 (1991).
27. A. Wasserman and M. Springford, *Physica* **B194–196**, 1801 (1994).
28. S. Dukan and Z. Tešanović, *Phys. Rev. Lett.* **74**, 2311 (1995).
29. M. G. Vavilov and Y. P. Mineev, *JETP* **85**, 1024 (1997).
30. L. P. Gor'kov and J. R. Schrieffer, *Phys. Rev. Lett.* **80**, 3360 (1998).
31. M. Tinkham, *Introduction to Superconductivity*, McGraw-Hill, New York (1975), p. 111.
32. G. D. Mahan, *Many-Particle Physics*, Plenum Press, New York (1981).
33. U. Brandt, W. Pesch, and L. Tewordt, *Z. Phys.* **201**, 209 (1967).
34. K. Ishida, H. Mukuda, Y. Kitaoka, K. Asayama, and Y. Ōnuki, *Z. Naturforsch* **51a**, 793 (1996).
35. M. Hedo, Y. Inada, E. Yamamoto, Y. Haga, Y. Ōnuki, Y. Aoki, T. D. Matsuda, H. Sato, and S. Takahashi, *J. Phys. Soc. Jpn.* **67**, 272 (1998).
36. M. Hedo, Y. Kobayashi, Y. Inada, E. Yamamoto, Y. Haga, J. Suzuki, N. Metoki, Y. Ōnuki, H. Sugawara, H. Sato, K. Tenya, T. Tayama, H. Amitsuka, and T. Sakakibara, *J. Phys. Soc. Jpn.* **67**, 3561 (1998).
37. C. Broholm, J. K. Kjems, W. L. Buyers, P. Matthews, T. T. M. Palstra, A. A. Menovsky, and J. A. Mydosh, *Phys. Rev. Lett.* **58**, 1467 (1987).
38. A. Krimmel, P. Fischer, B. Roessli, H. Maletta, C. Geibel, C. Schank, A. Grauel, A. Loidl and F. Steglich, *Z. Phys.* **B86**, 161 (1992).
39. K. Sugiyama, M. Nakashima, H. Ohkuni, K. Oda, K. Kindo, N. K. Sato, N. Kimura, T. Komatsubara, E. Yamamoto, Y. Haga, T. Honma, R. Settai, and Y. Ōnuki, *Physics of Strongly Correlated Electron Systems*, T. Komatsubara, H. Fujii, Y. Ōnuki, and H. Shiba (eds.), *Jpn. J. Appl. Phys. Series* **11**, 18 (1999).
40. S. A. Mentink, T. E. Mason, S. Süllow, G. J. Nieuwenhuys, A. A. Menovsky, and J. A. Mydosh, *Phys. Rev.* **B53**, R6014 (1996).
41. M. B. Maple, J. W. Chen, Y. Dalichaouch, T. Kohara, C. Rossel, and M. S. Torikachvii, *Phys. Rev. Lett.* **56**, 185 (1986).
42. W. K. Kwok, L. E. DeLong, G. W. Crabtree, and D. G. Hinks, *Phys. Rev.* **B41**, 11649 (1990).
43. J. P. Brison, N. Keller, P. Lejay, A. Huxley, L. Schmidt, A. Buzdin, N. R. Bernhoeft, I. Mineev, A. N. Stepanov, J. Flouquet, D. Jaccard, S. R. Julian, and G. G. Lonzarich, *Physica* **B199–200**, 70 (1994).
44. K. Matsuda, Y. Kohori, and T. Kohara, *J. Phys. Soc. Jpn.* **65**, 679 (1996).
45. S. Wüchner, N. Keller, J. L. Tholence, and J. Floquet, *Solid State Commun.* **85**, 355 (1993).
46. Y. Haga, T. Honma, E. Yamamoto, H. Ohkuni, Y. Ōnuki, M. Ito, and N. Kimura, *Jpn. J. Appl. Phys.* **37**, 3604 (1998).
47. Y. Ōnuki and T. Komatsubara, *J. Magn. Magn. Mater.* **63–64**, 281 (1987).
48. N. Keller, S. A. J. Wiegers, J. A. A. J. Berenboom, A. de Visser, A. A. Menovsky, and J. J. M. Franse, *J. Magn. Magn. Mater.* **177–181**, 298 (1998).
49. J. P. Brison, P. Lejay, A. Buzdin, and J. Flouquet, *Physica* **C229**, 79 (1994).
50. C. Geibel, C. Schank, S. Thies, H. Kitazawa, C. D. Bredl, A. Böhm, M. Rau, A. Grauel, R. Caspary, R. Helfrich, U. Ahlheim, G. Weber, and F. Steglich, *Z. Phys.* **B84**, 1 (1991).
51. Y. Haga, E. Yamamoto, Y. Inada, D. Aoki, K. Tenya, M. Ikeda, T. Sakakibara, and Y. Ōnuki, *J. Phys. Soc. Jpn.* **65**, 3646 (1996).
52. Y. Inada, A. Ishiguro, J. Kimura, N. Sato, A. Sawada, T. Komatsubara, and H. Yamagami, *Physica* **B206–207**, 33 (1995).
53. L. M. Sandratskii, J. Kübler, P. Zahn, and I. Mertig, *Phys. Rev.* **B50**, 15834 (1994).
54. K. Knöpfle, A. Mavromaras, L. M. Sandratskii, and J. Kübler, *J. Phys. Condens. Matter.* **8**, 901 (1996).
55. S. Koh, *Phys. Rev.* **B51**, 11669 (1995).
56. K. Satoh, T. Fujita, Y. Maeno, Y. Ōnuki, and T. Komatsubara, *J. Phys. Soc. Jpn.* **58**, 1012 (1989).